

Evaluation of the integration of the Wind-Induced Flutter Energy Harvester (WIFEH) into the built environment: Experimental and numerical analysis [☆]

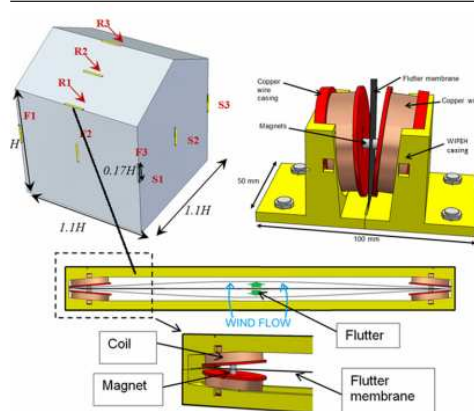
Angelo I. Aquino ^{*}, John Kaiser Calautit, Ben Richard Hughes

Department of Mechanical Engineering, University of Sheffield, Sheffield S10 2TN, UK

HIGHLIGHTS

- Investigation of WIFEH in wind tunnel and CFD of harvester-building were presented.
- Prototype was built and operation in various wind speeds was tested in wind tunnel.
- Impact of WIFEH locations and wind direction on speed at device were investigated.
- The roof apex showed the highest potential for power generation based on results.
- RMS and peak voltages and SC-current values were obtained for various wind speeds.

GRAPHICAL ABSTRACT



1

2 Abstract

3 With the ubiquity of low-powered technologies and devices in the urban environment
4 operating in every area of human activity, the development and integration of a low-
5 energy harvester suitable for smart cities applications is indispensable. The multitude
6 of low-energy applications extend from wireless sensors, data loggers, transmitters
7 and other small-scale electronics. These devices function in the microWatt-milliWatt
8 power range and will play a significant role in the future of smart cities providing power
9 for extended operation with little or no battery dependence. This study thus aims to
10 investigate the potential built environment integration and energy harvesting
11 capabilities of the Wind-Induced Flutter Energy Harvester (WIFEH) – a microgenerator
12 aimed to provide energy for low-powered applications. Low-energy harvesters such as
13 the WIFEH are suitable for integration with wireless sensors and other small-scale
14 electronic devices; however, there is a lack in study on this type of technology's
15 building integration capabilities. Hence, there is a need for investigating its potential
16 and optimal installation conditions.

17
18 This work presents the experimental investigation of the WIFEH inside a wind tunnel
19 and a case study using Computational Fluid Dynamics (CFD) modelling of a building
20 integrated with a WIFEH system. The experiments tested the WIFEH under various
21 wind tunnel airflow speeds ranging from 2.3 to 10 m/s to evaluate the induced
22 electromotive force generation capability of the device. The simulation used a gable-
23 roof type building model with a 27° pitch obtained from the literature. The atmospheric
24 boundary layer (ABL) flow was used for the simulation of the approach wind. The work

The short version of the paper was presented at ICAE2016 on Oct 8-11, Beijing, China. This paper is a substantial extension of the short version of the conference paper.

25 investigates the effect of various wind speeds and WIFEH locations on the
26 performance of the device giving insight on the potential for integration of the harvester
27 into the built environment. The WIFEH was able to generate an RMS voltage of 3 V,
28 peak-to-peak voltage of 8.72 V and short-circuit current of 1 mA when subjected to
29 airflow of 2.3 m/s. With an increase of wind velocity to 5 m/s and subsequent
30 membrane retensioning, the RMS and peak-to-peak voltages and short-circuit current
31 also increase to 4.88 V, 18.2 V, and 3.75 mA, respectively. For the CFD modelling
32 integrating the WIFEH into a building, the apex of the roof of the building yielded the
33 highest power output for the device due to flow speed-up maximisation in this region.
34 This location produced the largest power output under the 45° angle of approach,
35 generating an estimated 62.4 mW of power under accelerated wind in device position
36 of up to 6.2 m/s. For wind velocity (UH) of 10 m/s, wind in this position accelerated up
37 to approximately 14.4 m/s which is a 37.5% speed-up at the particular height. This
38 occurred for an oncoming wind 30° relative to the building facade. For UH equal to 4.7
39 m/s under 0° wind direction, airflows in facade edges were the fastest at 5.4 m/s
40 indicating a 15% speed-up along the edges of the building.

41 **Keywords**

42 Aero-elastic flutter; Buildings; Computational Fluid Dynamics (CFD); energy
43 harvesting; wind tunnel

44 **1. Introduction**

45 In this day and age, buildings are attributed for 20-40% of total world power
46 consumption. This is a figure greater than the consumptions of industry and transport
47 sectors [1]. Thus, new technologies that can mitigate the building sector power demand
48 are increasingly being advanced; one significant advancement being wind energy
49 technology. An important value of building-integrated wind energy harvesting is
50 bringing the power plant closer to the power consumers. With the public having better
51 power generation capabilities, people can also expect better energy efficiency and
52 reduced dependence to power companies, lower carbon footprint and general
53 stimulation of the economy. Moreover, this shift will decrease the load of the grid,
54 dependence on diesel generators in events of power outage and lower transmission
55 costs.

56
57 However, urban and suburban locations present problems for conventional building-
58 mounted turbines. There is the issue of significant turbulence in these areas, impeding
59 the turbines from harnessing laminar wind flow. In these conditions wind turbine
60 installers face insufficiency in analysing the more complex wind conditions. This leads
61 to problems of unfavourable turbine site selection leading to deficient power
62 production. Another issue that conventional rotational turbines face is the hazard of
63 having blades flying loose. These aspects add to the anxiety of turbine installation
64 among building owners, residents and stakeholders. However, perhaps the biggest
65 issue to building-integrated wind turbines (BIWT) is their cost-effectiveness. Smaller
66 wind turbines suitable for urban installations when installed onto buildings allow for a
67 higher cost-to-energy-production ratio.

68
69 A novel and emerging alternative to the conventional turbines are wind-induced flutter
70 energy harvesters. In this day and age, low-energy power generation devices have
71 been gathering increased attention because of their potential integration with self-

72 powered micro-devices and wireless sensor networks especially in the urban setting.
73 This is a primary motivation for this study. The power produced by these
74 microgenerators is sufficient to run light-emitting diodes, stand-alone wireless sensor
75 nodes and small liquid crystal displays [2]–[4]. Such devices like the Wind-Induced
76 Flutter Energy Harvester (WIFEH) as shown in Figure 1 can be in a form of a small-
77 scale wind generator that takes advantage of the flutter effect. Unlike turbine-based
78 generators, the WIFEH is a small-scale, light and inexpensive direct-conversion energy
79 harvester which does not use any gears, rotors or bearings. Wind flowing into and
80 around a tensioned membrane or belt causes it to flutter causing connected permanent
81 magnets to vibrate relative to a set of coils. This motion induces a current flowing in
82 the coil, thereby generating electric power.

83

84 Fig 1. Schematic diagram of a quad (4-coil arrangement) Wind-Induced Flutter
85 Energy Harvester (WIFEH)
86

87 The phenomenon of aero-elastic flutter describes self-feeding oscillations in which the
88 aerodynamic forces on a structure couple with its natural mode of oscillation thereby
89 producing rapid periodic movements. Flutter can occur to any structure exposed to
90 strong fluid flow, under the condition that a positive feedback response results between
91 the structure’s natural vibration and the acting aerodynamic forces [8].

92

93 Flutter on itself can be severely disastrous. Historic examples of flutter are the collapse
94 of Tacoma Narrows Bridge and that of Brighton Chain Pier. The structures failed due
95 to span failure caused by aero-elastic flutter [5]. However, this seemingly violent nature
96 of flutter can also be the foundation of its power when its potential for energy
97 harnessing is investigated. Flutter is classified under flow-induced vibrations, which is
98 an umbrella category that includes flutter-induced vibrations (FIV) [6]–[8] and vortex-
99 induced vibrations (VIV) [9]–[11].

100

101 Regular wind turbines generally don’t scale down well into smaller scales.
102 Nevertheless, flutter-based generators like the WIFEH can be designed to be suitable
103 for lighter applications. Low-energy flutter-based generators can operate in the range
104 of milliWatt to microWatt power generation. Although the power output is low, it has its
105 advantages compared to traditional wind turbines. The WIFEH is small, compact,
106 modular and suitable for turbulent flow, making it appropriate for partnering with
107 wireless sensor technologies – a field which has the greatest application potential for
108 this energy harvester [12]. Flutter energy harvesting is also not limited to
109 electromagnetic transduction, but can also be taken advantage of through the use
110 flexible piezoelectric membranes as demonstrated with an inverted flag harnessing
111 ambient wind to power a temperature sensor [13].

112

113 Recent world demand for wireless sensors is growing particularly in applications of
114 equipment supervision and monitoring focused on energy expenditure, usage, storage
115 and remote manipulation. The principal difficulties to what we call the “deploy-and-
116 forget” nature of wireless sensor networks (WSNs) are their restricted power capacity
117 and their batteries’ unreliable lifetimes. To surmount these problems, the area of
118 energy harvesting of ambient energy resources like air flow, water flow, vibrations, and
119 even radio waves has developed to be an encouraging new field. These and several

120 other types of ambient energy sources have been harnessed through various
121 technologies like thermomechanical, thermoelectric, photovoltaic and wind harvesting
122 technology [14]. There are even initiatives to develop micro-energy harvesters that can
123 harness both physical and chemical energies of the human body to power implanted
124 biomedical devices [15]. Along with developments in microelectronics, power
125 requirements for wireless sensor nodes keep on falling, varying presently from
126 microWatts to a few milliWatts [12].

127
128 In the year 2011, more than 1 million units of harvester modules were bought around
129 the world for building applications alone. This was mainly attributed to the expansive
130 network of wireless switches dedicated for lighting, air conditioning and sensors
131 detecting resident presence and determining ambient room conditions such as
132 humidity and temperature, mostly realised in commercial buildings. Running the
133 market growth of energy harvesters are the significant savings in installation costs and
134 maintenance-free operability due to little or no wire installation requirement [16].
135 Hence, novel methods should be established to further assess and optimise energy
136 harvester integration into the built environment. It has been shown that simple
137 configuration, low production cost and fast prototyping coupled with 3D-printing
138 technology all contribute to demonstrate practical applications of mini airflow-driven
139 energy harvesters in the urban setting [17].

140
141 In this paper, the evaluation of the energy harnessing potential of the WIFEH is
142 discussed. The evaluation is done two-fold: (i) through experimental investigation of
143 the harvester prototype conducted inside a wind tunnel; and (ii) through CFD analysis
144 relating external conditions and harvester location to harvester power generation
145 capabilities. The experimental analysis will assess a constructed WIFEH prototype's
146 performance when subjected to different wind tunnel airflow velocities. The prototype
147 will be centrally mounted with the membrane allowed to flutter in the wind thereby
148 inducing relative motion between fastened permanent magnets and a fixed conducting
149 coil. This motion in turn induces an electromotive force (voltage) in the conducting coil.
150 The (root-mean-square) RMS and peak-to-peak voltages and current readings will be
151 recorded through a memory-enabled digital oscilloscope and afterwards analysed and
152 discussed.

153
154 Brief review of previous works on the WIFEH exposed that several authors have
155 assessed the performance of the device in uniform flows in the laboratory or wind
156 tunnel but did not investigate the effect of buildings on its performance. Therefore it is
157 evident that there exists the necessity of investigating the integration of the WIFEH into
158 buildings using CFD analysis.

159
160 The CFD analysis will investigate the effect of various external conditions and device
161 locations on the performance of the WIFEH. The simulation will use a gable-roof type
162 building model with a 27° pitch. The atmospheric boundary layer (ABL) flow will be
163 used for the simulation of the approach wind. The three-dimensional Reynolds-
164 averaged Navier-Stokes (RANS) equations along with the momentum and continuity
165 equations will be solved using ANSYS FLUENT 16 for obtaining the velocity and
166 pressure field. Sensitivity analyses for the grid resolutions of the CFD simulations will
167 be performed for verification of modelling. In addition, the results of the flow around the

168 buildings and surface pressure coefficients will be validated with previous experimental
169 work. Figure 2 shows the overview of how this study is organised.

170
171

Fig. 2. General organisation of the study

172 Section 1 introduces the overview of the project, the motivation, challenges, a brief
173 background of the technology and the direction of the research. Section 2 presents the
174 review of related literature. Section 3 discusses the experimental aspect of the study
175 evaluating the technology prototype inside a wind tunnel, while Section 4 presents the
176 results of CFD analysis of the device integration into buildings. Section 5 highlights the
177 key findings.

178 **2. Literature Review**

179 In this section, various relevant energy harvester technologies for flow-induced flutter
180 focusing on the electromagnetic generation principle are reviewed.

181

182 Pimentel et al. [18] investigated the operation of a wind flutter harvester via
183 experimental testing. The evaluated device was 50-cm long and supported by a
184 Plexiglass frame, with a tensioned Mylar membrane installed with bolts on its ends.
185 This membrane had one side that is smooth while the other side was rough. This is
186 analogous to a simple aerofoil. The generator had an electromagnetic transducer
187 integrated in one end of the membrane. This transducer utilised two small neodymium
188 (NdFeB) magnets and a static coil situated adjacent to the magnets. Based on the
189 investigators' experimental results the minimum power output was 5 mW at wind speed
190 of 3.6 m/s and load resistance of 10 Ω ; the maximum power output was 171 mW under
191 airflow of 20 m/s, 110 Ω resistance and 38.1 N membrane tension.

192

193 Several parameters that affect the wind flutter harvester performance like membrane
194 tension, membrane length, magnet position and number of magnets were investigated
195 by Arroyo et al. [19] using experimental methods. The study highlighted the optimal
196 values for the key parameters, focusing on low wind speeds ranging from 1 to 10 m/s
197 but with powerful vibration acceleration. Dinh Quy et al. [20] studied a wind flutter
198 harvester with the magnet positioned centrally along the flexible membrane made of a
199 type of kite fabric called ripstop nylon fabric. The single unit micro generator was able
200 to produce power in the range of 3 - 5 mW. Five larger versions of these
201 microgenerators were combined to produce a "windpanel", which altogether were able
202 to deliver 30 to 100 mW of power at wind speeds less than 8 m/s. At low wind speeds
203 between 3 to 6 m/s, the output current is approximately 0.2 to 0.5 mA, the generated
204 voltage is between 2 to 2.5 V, and the generated power is about 2 to 3 mW, under
205 membrane oscillation frequency of approximately 5 Hz.

206

207 The earlier generations of flutter generators encountered practical problems as
208 identified by Fei et al. [21]. One example was the physical contact of the vibrating
209 membrane with the coils when its vibration amplitude is at an extreme high during
210 powerful winds. The placing of the magnets on the membrane should be thoroughly

211 tested to guarantee optimised magnetic flux undergone by the coils, which was also
212 addressed by Dinh Quy et al. [20].

213

214 To deal with these challenges and at the same time increase the efficiency of energy
215 harvesting by a fluttering belt, a novel variety of flutter-based resonant system was
216 proposed in [21] which involves of a shaft that acts as a support, an electromagnetic
217 resonator, a power management circuit, a super-capacitor for storage of charge and a
218 spring. A belt with dimensions 1 m long, 25 mm wide and 0.2 mm thick polymer was
219 used as the oscillating membrane. The electromagnetic resonator was positioned
220 close to the end of the membrane. This was the selected placement because of a
221 higher bending stiffness of the membrane close to the secured ends. This configuration
222 permitted a heavier magnet to be supported by the vibrating membrane [21]. The
223 super-capacitor is simply replaceable.

224

225 Dabin Zhu et al. [22] studied a device with an aerofoil linked to a beam which was
226 located next to a bluff body. This energy harvester worked under relatively low airflow
227 speed of 2.5 m/s and produced power of 470 μ W. The investigators found that a
228 drawback of this system was the factor that an initial displacement of the aerofoil was
229 required in order to be activated. Wang et al. [23] demonstrated a type of EMG-
230 resonant-cavity wind energy harvester integrated with dual-branch reed and tuning fork
231 vibrator. Their study emphasised the harvester's magnetic circuit being able to
232 increase the rate of change of magnetic flux. The tuning-fork mechanism of the
233 harvester was able to reduce system losses. Apex power output was measured to be
234 56 mW corresponding to a wind speed of 20.3 m/s with efficiency of energy conversion
235 of 2.3% at wind speed of 4 m/s. The experimental tests verified that the harvester can
236 operate in a wide range of wind speeds.

237

238

239 Two types of electromagnetic energy harvesters were investigated by Kim et al. [24]
240 which utilise direct airflow energy conversion to mechanical vibration - (i) a
241 wind-belt-like oscillatory linear energy collector specially for powerful air streams and
242 (ii) a harvester involving a Helmholtz resonator concentrated on harvesting energy
243 from weaker airflow like those found in environmental air streams. The moving part of
244 the harvester was made up of an oscillating membrane with secured permanent
245 magnets, positioned in the centre of the airflow. The second energy collector utilised a
246 Helmholtz resonator as an apparatus for concentrating oncoming wind flow. The wind-
247 belt-like oscillatory energy collector offered a peak-to-peak amplitude AC voltage of 81
248 mV at frequency of 530 Hz, generating this from an input of 50 kPa of pressure. The
249 Helmholtz-resonator-centred harvester provided a peak-to-peak amplitude AC voltage
250 of 4 mV at frequency of 1400 Hz, from 0.2 kPa pressure input, which corresponded to
251 5 m/s or 10 mph airflow speed.

252

253 It was demonstrated by Munaz et al. [25] that the energy generation of electromagnetic
254 energy harvester can be amplified by several factors through the introduction of
255 numerous magnets as the moving mass despite the fact that all other experimental
256 parameters were fixed. The harvester generated power of 224.72 μW in rectified DC
257 already, while having a load resistance of 200 Ω for a five-magnet setup. This
258 electromagnetic energy harvester operated at a low resonance frequency of 6 Hz,
259 which was envisioned by the investigators to be suitable for handheld devices and
260 remote sensing applications.

261

262 Energy harvesting through vibrations caused by the Karman vortex street through an
263 electromagnetic harvester was investigated by Wang et al. [6], with a device able to
264 produce instantaneous power of 1.77 μW when exposed to the vortex street. The open
265 circuit peak-to-peak voltage induced in the coil was measured to be approximately 20
266 mV. In the same investigation the researchers acknowledged that the vibrations from
267 other fluid flow can also be harnessed such as river currents, air flow from tire or fluids
268 inside machinery.

269

270 Kwon et al. performed an investigation for energy harvesting devices that use
271 T-shaped cantilever intended to accelerate the occurrence of aero-elastic flutter for low
272 wind speeds. The investigators studied two device types – one working through
273 piezoelectric effect while the other operates under electromagnetic induction principle.
274 For the electromagnetic energy converter the cantilever is permitted to undergo flutter
275 thereby causing the motion of magnets with respect to coils, producing electricity in the
276 conducting coils. The devices were tested inside a wind tunnel and it was observed
277 that the electromagnetic converter was able to generate a maximum of 1.2 mW of
278 power under 10 m/s wind speed, while the piezoelectric device provided 1.5 mW
279 maximum power [26].

280

281 Park et al. investigated a technology with a funnel that was intended to contract wind
282 flowing towards the energy harvester. The study noted that aero-elastic flutter
283 phenomenon only starts when airflow speed reaches a specific flutter onset speed and
284 when airflow is nearly perpendicular to the harvester. The investigators' solution was
285 to introduce a wind-flow-contracting funnel conceived to channel airflow to the flutter
286 energy converter and accelerate the airflow. The authors compared the device
287 performance under varying incident angles of wind and its effect on the voltage
288 generation for the device versions with funnel and without funnel. With the funnel, the
289 harvester produced almost a constant voltage even when the incident wind flow angle
290 varied. The initial CFD and wind tunnel results also exhibited that the funnel can
291 accelerate airflow speed by an estimated 20% within an incident angle of 30° [27].

292

293 In another study by Arroyo et al. two significant parameters namely the critical flutter
294 frequency and the critical wind speed as functions of the ribbon dimensions and
295 material properties were focused on through utilising both theoretical modelling and

296 experiments. The important finding was that from both simulation and experiments, the
297 critical speed increased when the dimensions were reduced. Therefore a device
298 designed for low-speed airflow has to take into account this increase through
299 marginally decreasing the ribbon tension since the higher the ribbon tension is, the
300 greater the airflow speed required to start fluttering [28].

301
302 No previous work reviewed the integration of low-energy flutter-induced harvesting
303 devices in buildings or structures. Most studies for these energy harvesters were
304 carried out in laboratory environments. There is also a lack in numerical investigations
305 about these energy harvesting technologies. There is a deficiency in research about
306 the applications of these harvesters in the urban environment. Most theoretical studies
307 employ unrealistic boundary conditions like the use of uniform flows. This study will
308 address this by conducting an urban flow simulation of a small building integrated with
309 low-energy wind-induced flutter energy harvester devices and evaluate the impact of
310 varying outdoor wind conditions.

311
312 Prior investigations about the building environment's potential for wind energy
313 harvesting underlined the necessity for detailed and precise analysis of wind flow
314 around buildings. To exploit the effect of wind acceleration above or around buildings
315 and to be able to determine the applicable type of wind energy technology to be
316 installed, appropriate integration analysis has to be conducted. In addition, there exists
317 the challenge of analysing the optimum placement of the wind energy harvesters.
318 Thorough simulations will lead to more data that can result to better installation
319 decisions [29].

320 **3. Performance evaluation of WIFEH prototype using wind tunnel testing**

321 To characterise the effect of various wind speeds to the harvester's performance, a
322 prototype was constructed and tested inside the wind tunnel. The prototype was tested
323 under varying wind tunnel airflow speeds to enable the measurement of RMS voltage,
324 peak-to-peak voltage and short-circuit current generated by the harvester in response
325 to the different wind velocities.

326
327 A full scale model of the WIFEH prototype was used in the experimental study. The
328 investigation was conducted in a low-speed closed-loop wind tunnel detailed in [30].
329 The wind tunnel had a test section with the dimensions of 0.5, 0.5, and 1 m (see
330 Figure 3). The variable intensity axial fan is capable of supplying wind speeds between
331 2.3 to 12 m/s. The flow in the wind tunnel was characterised prior to experimental
332 testing to indicate the non-uniformity and turbulence intensity in the test-section which
333 was 0.6% and 0.49% and according to the recommended guidelines [30].

334
335 Fig. 3. (a) Side view of the closed-loop wind tunnel (b) WIFEH prototype with one coil
336 configuration showing flutter motion at 2.3 m/s
337

338 The WIFEH system with one coil and eight stacked 1.5 mm-thick 10 mm-diameter
339 magnets was tested for preliminary experimental results inside the wind tunnel. The
340 prototype was positioned in a vertical orientation with terminals, as shown in Figure 4.

341 For data gathering, the system was connected to the digital oscilloscope positioned
342 outside the wind tunnel. It was ensured that the wind tunnel did not contain anything
343 except the WIFEH. The wind speed inside the tunnel was varied from the wind tunnel
344 minimum of 2.3 m/s to maxima of (i) 8 m/s without belt retensioning and (ii) 10 m/s with
345 belt retensioning. It should be noted that without retensioning, the performance of the
346 belt did not improve beyond 8 m/s. Without membrane retension there was observed
347 self-sustained but unstable oscillations leading to irregular voltage signal readings.
348

349 Fig. 4. Schematic of WIFEH prototype in the wind tunnel test section
350

351 The WIFEH was then connected to the Tektronix Oscilloscope to measure, display and
352 record the system's AC (Alternating Current) voltage output. This is depicted in
353 Figure 5. The voltage waveform relevant characteristics such as the maximum value,
354 peak-to-peak voltage, root-mean-square (RMS) voltage and frequency could be
355 observed instantaneously in the 7-inch WVGA TFT colour display monitor. The
356 Tektronix TBS1052B Digital Storage Oscilloscope model is capable of up to 1 GS/s
357 sampling rate, bandwidths of 50 - 200 MHz and has a dual channel frequency counter.
358 The instrument has 3% vertical (voltage) measurement accuracy permitting the user
359 to see all signal details and obtain the stated real-time sampling rate on all channels
360 all the time with at least 10X over sampling; sampling performance is not reduced when
361 changing the horizontal (time) scale. The oscilloscope has two probes that were
362 attached to the two ends of the coils of the energy harvester, with one probe also
363 connected to the ground, to measure the potential difference between two points at
364 each specific time. Measurements were taken uninterruptedly producing a continuous
365 waveform that is displayed in oscilloscope's LCD monitor and were recorded in a
366 storage device connected to the oscilloscope USB port.
367

368 Fig. 5. Schematic of the coil connections to the oscilloscope
369

370 The WIFEH model used for the wind tunnel testing was partially constructed using 3D
371 printing. The schematic diagram of the two-coil prototype system is shown in Figure 6.
372 The copper wire used to make the conducting coil is enamelled copper wire 40 SWG
373 (Standard Wire Gauge) with 0.125 mm diameter. It is packaged as grade 1 enamelled
374 copper wire in a roll of 250 grams and is suitable for coil forming. This copper wire is
375 tested based on the standards of IEC 851/5/4 having a threshold energy transfer rate
376 of 7 kVA (kilovolt-Amperes). The circular casing was 3D-printed using HP Designjet
377 3D Printer. The outer diameter of the casing is 54 mm and the inner diameter (hole
378 diameter) is 12.5 mm, with outer thickness of 20 mm and inner spacing for the coil
379 winding of 12 mm. The two ends of the coil wire were soldered onto insulated jumper
380 lead wires for more convenient connections to the load (LED) for initial testing of
381 generation, circuit board or testing apparatus. Approximately 2500 turns were looped
382 to produce the coil. The internal resistance of the coil is 1150 Ohms.
383

384 The flexible membrane is made of a two layer construction: a weather-resistant outer
385 shell and reinforced fabric backing. It resists moisture, UV rays and extreme
386 temperature. The backing material provides strength due to the tight weave. It adheres
387 to metallic objects well. It is highly suitable to hold the magnets in place, sturdy but light
388 and highly flexible allowing flutter to occur. In the tests it has not let the magnets fall
389 off in any trial done. A 1 cm wide section of the tape material of which 0.5 m in length
390 was exposed to airflow was used for the harvester. These dimensions were observed

391 to be suitable for the flutter occurrence to be initiated with the given load of the magnets
392 while keeping the use of the tape material economically, thereby reducing its weight.

393
394 Neodymium N52 type disk magnets were used to generate the magnetic fields that are
395 going to interact with the conducting coils. The magnets have a diameter of 10 mm and
396 a thickness of 1.5 mm. N52 is the highest grade for magnets that are widely available.
397 In a size for size comparison an N52 grade magnet will have approximately 35% more
398 pull power than the same sized N35 grade magnet. This type of magnet is axially
399 magnetised through the thickness producing one surface as the North pole and the
400 other surface being the south pole. Each unit weighs 0.09 g and has a coating of Ni-
401 Cu-Ni layers (Nickel-Copper-Nickel). The calculated maximum vertical hold of each
402 magnet is 206 g, having a theoretical maximum pull of 1033 g. The maximum operating
403 temperature of this type of magnet is 80°C, beyond which it will start to lose part of its
404 magnetisation. Four units of the 1.5 mm thick magnets were stacked together which
405 are then attached to the adhesive side of the belt. It was estimated that four stacked
406 magnets will possess sufficient magnetic field strength strong enough to generate
407 substantial induction in the coils but at the same time not too heavy to hinder the belt
408 flutter motion. To balance the four magnets on one side, another four were attached
409 on the other side of the membrane with the opposite pole facing the first magnets stack
410 so that the magnetic attraction kept the two magnet groups in place.

411
412 Fig. 6. Schematic and dimensions of 3D-printed WIFEH prototype

413
414 The AC Voltage waveform produced by the WIFEH system when subjected to a
415 constant airflow of 2.3 m/s is shown in Figure 7, forming a regular pattern of sinusoidal
416 wave. This first trial corresponds to the initial and minimum flow velocity of the wind
417 tunnel. The root-mean-square (RMS) voltage was measured to be 3.00 V. The RMS
418 voltage is the effective value of a varying voltage source such as the WIFEH. The rated
419 output of most power supplies are expressed in RMS AC voltage (e.g. 110 / 230 V wall
420 socket output is RMS value). The maximum voltage reading was 3.84 V while the peak-
421 to-peak voltage was 8.72 V.

422
423 Fig. 7. Open-circuit voltage of the Wind-Induced Flutter Energy Harvester (WIFEH)
424 without membrane retensioning under 2.3 m/s flow velocity

425
426 Without prior retensioning the membrane, the wind tunnel airflow speed was increased
427 to 5 m/s and the AC voltage signal was again observed and recorded as shown in
428 Figure 8. The waveform is not as regular as for the previous case and we can observe
429 more occurrences of sharper turns with resemblance to sawtooth signals, with
430 decreasing magnitude of the negative peaks of the signal. The recorded RMS for 5
431 m/s wind speed is 4.16 V with peak-to-peak value 18.4 V and maximum value of 8.8 V.

432
433 Fig. 8. Electrical signal open-circuit voltage of the Wind-Induced Flutter Energy
434 harvester (WIFEH) without membrane retensioning under 5m/s flow velocity

435
436 The membrane of the WIFEH was then retensioned while maintaining the wind tunnel
437 airflow speed of 5 m/s. The AC Voltage waveform produced by the harvester system
438 when subjected to a constant airflow was again recorded. A regular pattern of
439 sinusoidal wave with minor and major peaks was again observed. Under this wind

440 condition, the microgenerator generated an RMS voltage of 4.88 V with maximum of
441 9.20 V and peak-to-peak value of 18.2 V. This is shown in Figure 9.

442
443 Fig. 9. Electrical signal open-circuit voltage of the Wind-Induced Flutter Energy
444 Harvester (WIFEH) with membrane retensioning under 5 m/s flow velocity
445

446 Incremental increases of 1 m/s airflow speed were also conducted for two cases: (i)
447 without belt retensioning (see Figure 10) and (ii) with belt retensioning (see Figure 11),
448 starting from 2.3 m/s. The open-circuit voltage and short-circuit current were then
449 observed using a digital multimeter after each incremental increase. The digital
450 multimeter used was the Proster VC99. It is an auto-ranging digital multimeter capable
451 of measuring AC/DC voltage and current, resistance, frequency and duty cycle, which
452 provides an LCD display.

453
454 It can be observed that for the case without belt retensioning the maximum open-circuit
455 voltage and short-circuit current both occurred for 6 m/s airflow speed, beyond which
456 there was a significant drop in both variables. This was due to the observation that
457 beyond said airflow speed the belt started to perform less stable oscillations compared
458 to cases of lower wind speeds. This unstable flutter greatly influences the magnets-
459 coil relative dynamic positioning, therefore affecting the induced voltage and current in
460 the conducting coil. Thus the relationship between airflow speed and open-circuit
461 voltage or short-circuit current was not observed to be linear (Figure 9). However, with
462 retensioning of the belt the linear relationship between airflow and voltage / current
463 resumed as can be seen in Figure 10. The trend continued even up to 10 m/s airflow
464 speed.

465
466 Fig. 10. Electrical output performance of the WIFEH without retensioning under
467 various flow velocities: (a) Open-circuit voltage (b) Short-circuit current
468

469
470 Fig. 11. Electrical output performance of the WIFEH with retensioning under various
471 flow velocities: (a) Open-circuit voltage (b) Short-circuit current
472

473 **4. Computational Fluid Dynamics (CFD) analysis of WIFEH integration into** 474 **buildings**

475 The basic assumptions for the numerical simulation include a three-dimensional, fully
476 turbulent, and incompressible flow. The flow was modelled by using the standard
477 k-epsilon turbulence model, which is a well-established method in research on wind
478 flows around buildings [31], [32]. The CFD code was used with the Finite Volume
479 Method (FVM) approach and the Semi-Implicit Method for Pressure-Linked Equations
480 (SIMPLE) velocity-pressure coupling algorithm with the second order upwind
481 discretisation. When the flow is not aligned with respect to the grid, more accurate
482 results are generally obtained by using the second order discretisation, especially
483 when dealing with complex flows. The general governing equations include the
484 continuity, momentum and energy balance for each individual phase. The standard k-
485 e transport model was used to define the turbulence kinetic energy and flow dissipation
486 rate within the model. The governing equations for the mass conservation (eqn. 1),
487 momentum conservation (eqn. 2), energy conservation (eqn. 3), turbulent kinetic
488 energy (TKE) (eqn. 4) and energy dissipation rate (eqn. 5) are summarised below:

$$\frac{\partial \rho}{\partial t} + \nabla \times (\rho u) = 0 \quad (\text{eqn.1})$$

490 where ρ is density, t is time and u is fluid velocity vector.

$$\frac{\partial(\rho u)}{\partial t} + \nabla \times (\rho u u) = -\nabla p + \rho g + \nabla \times (\mu \nabla u) - \nabla \times \tau_t \quad (\text{eqn.2})$$

491 where p is the pressure, g is vector of gravitational acceleration, μ is molecular dynamic
492 viscosity and τ_t is the divergence of the turbulence stresses which accounts for
493 auxiliary stresses due to velocity fluctuations.

$$\frac{\partial(\rho e)}{\partial t} + \nabla \times (\rho e u) = \nabla \times (k_{eff} \nabla T) - \nabla \times \left(\sum_i h_i j_i \right) \quad (\text{eqn.3})$$

494 where e is the specific internal energy, k_{eff} is the effective heat conductivity, T is the air
495 temperature, h_i is the specific enthalpy of fluid and j_i is the mass flux.

$$\frac{\partial(\rho k)}{\partial t} + \nabla \times (\rho k u) = \nabla \times [\alpha_k \mu_{eff} \nabla k] + G_k + G_b - \rho \varepsilon \quad (\text{eqn.4})$$

$$\frac{\partial(\rho \varepsilon)}{\partial t} + \nabla \times (\rho \varepsilon u) = \nabla \times [\alpha_\varepsilon \mu_{eff} \nabla \varepsilon] + C_{1\varepsilon} \frac{\varepsilon}{k} (G_k + C_{3\varepsilon} G_b) - C_{2\varepsilon} \rho \frac{\varepsilon^2}{k} \quad (\text{eqn.5})$$

496 where G_k is the source of TKE due to average velocity gradient, G_b is the source of TKE
497 due to buoyancy force, α_k and α_ε are turbulent Prandtl numbers, $C_{1\varepsilon}$, $C_{2\varepsilon}$ and $C_{3\varepsilon}$ are
498 empirical model constants.

499 The geometry (Figure 12) was created using commercial CAD software and then
500 imported into ANSYS Geometry (pre-processor) to create a computational model. The
501 shape of the building was based on [32], which is a gable roof type building with a roof
502 pitch of 26.6°. The overall dimension of the building was 3.3 m (L) x 3.3 m (W) x 3 m
503 (H). To create a computational domain, the fluid volume was extracted from the solid
504 model as shown in Figure 13. The fluid domain consisted of an inlet on one side of the
505 domain, and an outlet on the opposing boundary wall. The simulations were completed
506 using parallel processing on a workstation with two Intel Xeon 2.1 GHz processors and
507 16 GB fully-buffered DDR2 memory.

508

509

Fig. 12. CAD geometry of building with WIFEH devices

510 The computational domain size and location of model were based on the guideline of
511 COST 732 [33] for environmental wind flow studies. According to the guidelines, for a
512 single building with the height H , the horizontal distance between the sidewalls of the
513 building and side boundaries of the computational domain should be $5H$. Similarly, the
514 vertical distance between the roof and the top of domain should also be $5H$. In the flow
515 direction, the distance between the inlet and the façade of the building should be $5H$
516 while for the leeward side and outlet, it should be $15H$ to allow the flow to re-develop
517 behind the wake region, as fully developed flow is normally assumed as the boundary
518 condition in steady RANS calculations [33].

519

520

Fig. 13. Computational domain of building with WIFEH devices

522 4.1 Mesh design and verification

523 Due to the complexity of the model, a non-uniform mesh was applied to volume and
 524 surfaces of the computational domain [34], [35]. The generated computational mesh
 525 of the building model is shown in Figure 14. The grid was modified and refined
 526 according to the critical areas of interests in the simulation such as the WIFEH. The
 527 size of the mesh element was extended smoothly to resolve the areas with high
 528 gradient mesh and to improve the accuracy of the results. The inflation parameters
 529 were set according to the complexity of the geometry face elements, in order to
 530 generate a finely resolved mesh normal to the wall and coarse parallel to it [36].

531

532 Fig. 14. (a) Computational grid (b) Sensitivity analysis

533

534 In this study, Grid Convergence Method (GCI) method was used to verify the
 535 computational modelling of the building integrated with the WIFEH. The computational
 536 grid was based on a sensitivity analysis which was performed by conducting additional
 537 simulations with same domain and boundary conditions but with various grid sizes.
 538 The process increased the number of elements between 2.44 (coarse), 3.8 million
 539 (medium) and 4.90 million (fine). The computational time associated with running the
 540 simulations (converged) with coarse, medium and fine mesh were 5 hours, 8 hours
 541 and 10 hours, respectively. The grid resolution was determined taking into account an
 542 acceptable value for the wall y^+ . The log-law, which is valid for equilibrium boundary
 543 layers and fully developed flows, provides upper and lower limits of the acceptable
 544 distance between the near-wall cell centroid and the wall. The distance is usually
 545 measured in the dimensionless wall units, y^+ . The average y^+ values over the
 546 windward and the leeward roofs were about 70 and 25 for the coarser grid, and about
 547 35 and 15 for the finer grid, respectively. The Grid Convergence Method (GCI) method
 548 (based on the Richardson extrapolation method) was selected to estimate the
 549 uncertainty due to discretisation [37]–[39]. The procedure detailed in [38] was followed
 550 and is summarised below:

551 The first step is to define a representative grid size h .

$$h = \left[\frac{1}{C} \sum_{i=1}^C (\Delta V_i) \right]^{1/3} \quad (\text{eqn.6})$$

552 where C is the total number of cells used for the 3D computations and ΔV_i is the
 553 volume.

554 The next step is to select three significantly different set of grids, C and run simulations
 555 to determine the values of key variables, ϕ . In this case, the average value of the
 556 airflow velocity in the vertical line in the R1 device was selected as the variable. The
 557 size of the grids were C_1 (5.90 million), C_2 (3.50 million) and C_3 (2.00 million), giving
 558 r values of 1.30 and 1.32.

559 The next step is to calculate the apparent order, p of the method using the next
 560 equation. The equation was solved using fixed point iteration, with the initial guess
 561 equal to the first term [38].

$$p = \frac{1}{\ln(r_{21})} |\ln|\varepsilon_{32}/\varepsilon_{21}| + q(p)| \quad (\text{eqn.7})$$

$$q(p) = \ln\left(\frac{r_{21}^p - [1 \times \text{sgn}(\varepsilon_{32}/\varepsilon_{21})]}{32 - [1 \times \text{sgn}(\varepsilon_{32}/\varepsilon_{21})]}\right) \quad (\text{eqn.8})$$

562 where $\varepsilon_{32} = \phi_3 - \phi_2$ and $\varepsilon_{21} = \phi_2 - \phi_1$.

563 Finally, the approximate relative error e_a^{21} , extrapolated relative error ϕ_{ext}^{21} and fine-grid
 564 convergence index GCI_{fine}^{21} (eqn.10) are calculated.

565 Table 1 shows examples of the calculation procedure for the three selected grids.
 566 According to Table 1, the numerical uncertainty in the fine-grid solution for the velocity
 567 at 3.012m was 2.68% which corresponded to ± 0.10 m/s.

568 Table 1. Sample calculations of discretisation error using the GCI method

569 Figure 15 (a) shows the vertical velocity profiles (line with 18 equally distributed points)
 570 drawn from the R1 device, which was based on the three set grids. In addition, the
 571 extrapolated values, ϕ_{ext}^{21} are also plotted and was calculated using the following
 572 equation:

$$\phi_{ext}^{21} = (r_{21}^p \phi_1 - \phi_2) / (r_{21}^p - 1) \quad (\text{eqn.9})$$

573 The local order of accuracy p ranged from 0.95 to 16.1. The average apparent order
 574 of accuracy was used to assess the GCI index values in eqn.11, which is plotted in
 575 the form of error bars, as shown in Figure 4b. Based on the fine-grid convergence
 576 index, the maximum discretisation uncertainty was 5.87%. The discretisation
 577 uncertainty value ranged from 0.31% to 6.61%, with a global average of 1.52%.

$$GCI_{fine}^{21} = \frac{1.25e_a^{21}}{r_{21}^p - 1} \quad (\text{eqn.10})$$

578 Fig. 15. Grid verification using the Grid Convergence (GCI) method. (a) plot of the
 579 velocity profiles drawn from a line in the R1 device; (b) fine grid solution, with
 580 discretisation error bars computed using the GCI index.

581 4.2 Boundary conditions

582 The boundary conditions were specified according to the AIJ guidelines [40]. The
 583 profiles of the airflow velocity U and turbulent kinetic energy (TKE) were imposed at
 584 the inlet which were based on [32], with the stream-wise velocity of the approaching
 585 flow obeying the power law with an exponent of 0.25 which corresponds to a sub-urban
 586 terrain (See Figure 16). The values of ε for the k-epsilon turbulence model were
 587 acquired by assuming local equilibrium of $P_k = \varepsilon$ [32]. The standard wall functions [41]
 588 were applied to the wall boundaries except for the ground, which had its wall functions
 589 adjusted for roughness [42]. According to [42], this should be specified by an equivalent

590 sand-grain roughness height k_s and a roughness constant C_s . The horizontal non
591 homogeneity of the ABL was limited by adapting sand-grain roughness height and
592 roughness constant to the inlet profiles, following the equation of [43] :

593
$$k_s = \frac{9.793z_0}{C_s} \quad (\text{eqn.11})$$

594 where z_0 is the aerodynamic roughness length of the sub-urban terrain. The values
595 selected for sand-grain roughness height and a roughness constant 1.0 mm and 1.0
596 [32]. The sides and the top of the domain were set as symmetry, indicating zero normal
597 velocity and zero gradients for all the variables at the side and top wall. For the outlet
598 boundary, zero static pressure was used. The boundary conditions for the CFD model
599 are summarised in Table 2.

600
601
602 Fig. 16. (a) Velocity profile (b) TKE profile of approach wind flow [32]
603

604
605 Table 2. Summary of the CFD model boundary conditions
606

607
608 The convergence of the solution and relevant variables were monitored and the
609 solution was completed when there were no changes between iterations. In addition,
610 the property conservation was also checked if achieved. This was carried out by
611 performing a mass flux balance for the converged solution. This option was available
612 in the FLUENT flux report panel which allows computation of mass flow rate for
613 boundary zones. For the current simulation, the mass flow rate balance was below the
614 required value or <1% of smallest flux through domain boundary (inlet and outlet).

615 4.3 Method verification and validation

616 Figure 17 shows a comparison of the result of different turbulence model (k-epsilon
617 standard, k-epsilon realizable and k-omega) for the velocity profile drawn from the
618 vertical line in the R1 device. It can be observed that the k-epsilon standard curve lies
619 between the plots of k-epsilon realizable and k-omega, which is especially noticeable
620 between the heights of 3.005 and 3.015 m. It is obvious that there is an occurring
621 speed-up within the interior zone of the WIFEH device regardless of the turbulence
622 model used, as can be observed from Figure 17 (b). Although shifting to the k-omega
623 model could potentially affect the performance results of the WIFEHs located in the
624 leeward side of the building; a higher set of velocity results could be generated leading
625 to greater output for the devices in case of k-omega model.

626 As observed in Figure 17 (a), a very similar trend can be noticed for different turbulence
627 models particularly the k-epsilon standard and realizable with an average error of 3.9%
628 between the points. The average error between k-epsilon standard and k-omega was
629 6.44. From the velocity contours shown in Figure 17 (b) it can be noticed that the
630 k-epsilon standard model also displays more distinguishable and more evenly
631 distributed velocities at a lower speed at the wake of the flow behind the structure,
632 compared to the k-omega model. The k-epsilon model provides the standard, mostly
633 accepted results and is more suitable when studying free-shear layers and wake zones
634 while the standard k-omega model is more suitable in the near wall boundary regions.
635

636

637

638 Fig. 17. Sensitivity analysis of turbulence model (a) velocity profile in R1 (b) velocity
639 contours

640

641 Figure 18 (a) and (b) show a comparison between the experimental PIV results of [32]
642 and the current modelling results of the velocity distribution around the building model.
643 The results of the airflow velocity close to the windward wall seem to be at a lower
644 speed in the model compared to the PIV results, however a similar pattern was
645 observed for most areas particularly close to the roof. Figure 18 (c) and (d) show a
646 comparison between the prediction of the current model and [32] of the pressure
647 coefficient distribution around the building model. It is to be noted that the contour of
648 Figure 18 (a) also apply to that of (b), while that of Figure 18 (c) apply to (d).

649

650 Fig. 18. (a) PIV measurements of velocity [32] (b) velocity distribution in the current
651 model (c) pressure coefficient result [32] (d) pressure coefficient distribution in the
652 current model

653 4.4 CFD results and discussion

654 The system of the aero-elastic belt energy harvester integrated into a building was
655 modelled using CFD through ANSYS Fluent simulating the airflow pattern, velocity
656 magnitude and distribution around the building and within and surrounding the energy
657 harvester. This was conducted to allow for optimisation of the positioning of the energy
658 harvester throughout the various building sections. This investigation simulated a
659 gentle breeze, which is category 3 in the Beaufort wind force scale.

660

661 Figure 19 shows the velocity contours of a side view cross-sectional plane inside the
662 computational domain representing the airflow distribution around the building
663 integrated with WIFEH. The left hand side of the plot shows the scale of airflow velocity
664 in m/s. The contour plot in the fluid domain is colour coded and related to the CFD
665 colour map, ranging from 0 to 5.9 m/s. As observed, the approach wind profile entered
666 from the right side of the domain and the airflow slowed down as it approached the
667 building and lifted up. Separation zones were observed on the lower windward side of
668 the building and also at the leeward side of the building and roof. Zoomed in views of
669 the velocity distribution around the WIFEH devices R1, R2 and R3 are shown on top
670 of the diagram. The results showed that the shape and angle of the roof had a
671 significant impact on the performance of the WIFEH. In the diagram, it is clear that
672 locating the device at the leeward side of the roof will result in little to no energy
673 generation due to the low wind speeds in this area. However, it should be noted that
674 this was not the case for other wind angles, for example when the wind is from the
675 opposite direction. Therefore, location surveying, wind assessment and detailed
676 modelling are very important when installing devices in buildings. At wind velocity (U_H)
677 4.7 m/s and 0° wind direction, the airflow speed in R1 was the highest at 4.5 m/s while
678 the lowest was observed for the R2 WIFEH located at the centre of the roof.

679

680 Fig. 19. Contours of velocity magnitude showing a cross-sectional side view of the
681 building

682

683 Figure 20 displays the velocity contours of a top view cross-sectional plane inside the
684 computational domain representing the airflow distribution around the building
685 integrated with WIFEH. The approach wind profile entered from the right side of the
686 domain and the airflow slowed down as it approached the building and accelerated as
687 it flowed around the corners. Separation zones were observed on the leeward side of
688 the building and also the sides. Zoomed in views of the velocity distribution around the
689 WIFEH devices F1-F3 and S1-S3 are shown on top and right side of the diagram. At
690 wind velocity (U_H) 4.7 m/s and 0° wind direction, the airflow speed in F1 and F3 were
691 the highest at 5.4 m/s while the lowest was observed for the S2 and F2 WIFEH located
692 at the airflow recirculation zones.

693 Fig. 20. Contours of velocity magnitude showing a cross-sectional top view of the
694 building

695 Figure 21 compares the maximum air velocity speed measured at the belt location for
696 roof installations R1, R2 and R3 at various wind directions. These setups behaved in
697 a trend similar to each other, but the notable highest velocities were attained from the
698 R3 or apex installation. These setups had peak velocity values occurring at the region
699 between 30° to 60° orientation, with the maximum value obtained at 30° . There was
700 significant speed decrease after 60° that could be attributed to the belt frame corners
701 which impeded the wind from flowing through the belt region and therefore would
702 reduce its performance or not allow the belt to flutter

703 Fig. 21. Effect of wind direction on the wind speed at WIFEH located on the roof for
704 various wind angle of approach with outdoor wind $U_H = 10$ m/s

705
706 Figures 22 and 23 compare the maximum air velocity speed measured at the device
707 location for the windward and side installations, respectively at various wind directions.
708 When comparing the two figures it was observed that the plot of F3 had a similar trend
709 with the S1 device which showed a significant performance drop in terms of velocity
710 between 20 - 60° . This was also due to the frame of the WIFEH which impeded the wind
711 from flowing through the belt region and therefore would reduce its performance or not
712 allow the belt to flutter.

713
714 While the plot of F1 was a mirrored of S3, and F2 was mirrored S2. There is some
715 symmetry that can be expected as observing the locations in Figure 12. It is not a
716 perfect symmetry due to the roof shape having some effect on airflow. Looking at the
717 location with highest velocity values for the front side of the building, there was a
718 significant decrease in velocity from 10° to 40° , accounting for approximately 83%
719 speed reduction, and same increase in speed was observed from 40° to 70° . For the
720 side installation S1 the tipping point was at 50° where the change in angle exposure
721 past this point marked significant increase in velocity. From the results it was clear that
722 both the location of the device and wind direction had a significant effect on the air
723 speed achieved at the device location. Therefore a complete detailed analysis of these
724 factors should be carried out when integrating WIFEHs to buildings to ensure that the
725 performance is optimised.

726 Fig. 22. Effect of wind direction on the wind speed at WIFEH located on the windward
727 side of building with outdoor wind at $U_H = 10$ m/s

728 Fig. 23. Effect of wind direction on the wind speed at WIFEH located on the side of
729 building with outdoor wind at $U_H = 10$ m/s

730
731 Figure 24 illustrates the effect of different outdoor wind speed U_H values of 2, 4, 6, 8,
732 and 10 m/s at 0° wind direction on the air speed achieved at the device location. Similar
733 trend was observed for all the curves with the highest speed achieved in R1 and F3
734 and lowest speed achieved in F2 and S2. The increase in the velocity profile
735 corresponded to a proportional increase for the wind speed for all the device
736 locations.

737
738 Fig. 24. Wind speeds gathered at WIFEH position for various mounting locations for
739 0° wind angle of approach

740
741 Figure 25 depicts velocity results for 90° wind angle approach. At this angle the output
742 of the roof installations were overtaken by those in the front and side, most notably by
743 F3, S1 and S3 mainly because of the geometry of the device frame. The frame restricts
744 airflow in the perpendicular direction to the device. Therefore for locations with this
745 type of prevailing wind direction it will be better for the WIFEH to be integrated through
746 the front and side edges of the building.

747
748 Fig. 25. Wind speeds gathered at WIFEH position for various mounting locations for
749 90° wind angle of approach

750
751 Figure 26 compares the estimated output of the device at various locations and wind
752 directions of 0 to 90° , in increments of 10 degrees while maintaining a uniform outdoor
753 wind velocity ($U_H = 10$ m/s). F1, F2 and F3 represent the WIFEH devices mounted on
754 the front face of the building; S1, S2 and S3 represent those on the side face, while
755 R1, R2 and R3 are those for the roof locations. As observed, the highest power output
756 comes from location R3 – the apex of the building – with an estimated output of 15.2
757 V, resulting from wind speed that accelerated up to approximately 14.4 m/s,
758 approximately 37.5% speed-up at the particular height. This occurred for an incoming
759 wind 30° relative to the building facade.

760
761 Depending on prevailing wind direction of the area, the installation location of the
762 device can be determined. The green trendline represents the power output trend for
763 R3, the location with the highest total power generation summed over 0 to 90 degrees.
764 The brown trendline shows the trend for S2, the location with the lowest summed power
765 generation over the same angular range.

766
767 Secondary to the building apex, locations on the edge also provide well above-average
768 power output. Based on the simulated conditions, locations S3, F1 and R1 should be
769 optimum locations for building integration of the WIFEH, considering the power
770 averages for 0, 45 and 90-degree orientations.

771
772 The last locations an installer would want to put an WIFEH on are the central areas of
773 the building's faces (illustrated by F2 and S2). Taking into account angular averages

774 these locations provided the least amount of power, with no power generated at all for
775 some cases due to the wind speed not being able to make it to the WIFEH's cut-in
776 wind speed for generation. This finding can be considered by some to be a
777 counterintuitive result, considering these locations are directly hit by the oncoming
778 wind.

779 Fig. 26. Sample calculation of estimated voltage output based on WIFEH (2-magnet-
780 coil system)

781
782 Figure 27 compares the estimated output of the device located in the three locations
783 F3, S3 and R3 at various outdoor wind speeds. Among these three locations, at 30°
784 wind direction, R3 provided the highest output ranging between 2.5 to 15.2 V, while F3
785 showed the lowest output.
786

787 Fig. 27. Impact of various outdoor wind speeds (U_H) on the estimated output of the
788 WIFEH for locations F3, S3 and R3

789
790 From the results it was clear that both the location of the device and wind direction had
791 significant effects on the air speed achieved at the belt locations. Therefore a complete
792 and detailed analysis of these factors should be carried out when integrating aero-
793 elastic belts to buildings to ensure that the performance is optimised. Certain changes
794 in angle exposure past certain critical values marked significant increase in velocity
795 and consequently, power generation.

796 5. Conclusions and future works

797 The Wind-Induced Flutter Energy Harvester is valuable for low-energy wind harvesting
798 in the built environment due to its low cost and modularity. The following points
799 encapsulate the important findings of the study:

- 800 • With increasing airflow speed came increases in open-circuit voltage and short-
801 circuit current produced by the WIFEH. Regular sinusoidal waveform voltage
802 signals were observed through a digital oscilloscope for wind tunnel airflow
803 speeds of 2.3 m/s and 5 m/s with the belt retensioned.
- 804 • The RMS (effective) voltages recorded were 3.0 V and 4.88 V with maximum
805 values of 3.84 V and 9.20 V for 2.3 m/s and 5 m/s wind tunnel airflow speeds,
806 respectively.
- 807 • The simulation used a gable-roof type building model with a 27° pitch obtained
808 from the literature. The atmospheric boundary layer (ABL) flow was used for the
809 simulation of the approach wind. At wind velocity (U_H) 4.7 m/s and 0° wind
810 direction, the airflow speed in R1 was the highest for the roof section at 4.5 m/s.
811 At wind velocity (U_H) 4.7 m/s and 0° wind direction, the airflow speed in F1 and
812 F3 were the highest for the façade and side sections at 5.4 m/s.
- 813 • The overall highest power output comes from location R3 – the apex of the
814 building – with an estimated output of 15.2 V, resulting from wind speed that
815 accelerated up to approximately 14.4 m/s, approximately 37.5% speed-up at
816 the particular height. This occurred for an incoming wind 30° relative to the
817 building facade.

- 818 • Optimum installation of the WIFEH devices translates to prioritising the roof and
819 the trailing edges of the building to yield the highest possible power generation,
820 depending on wind conditions, while avoiding the leading edge or centres of
821 surfaces.

822
823 Future studies on the installation of the WIFEH in buildings will include simulations
824 using transient models that will also involve non-uniform flow conditions. Prospective
825 investigations on the impact of varying shapes of the subject building and different
826 locations of the device located on these new surfaces will also be conducted. Further
827 investigations will also include the impact of surrounding buildings on the performance
828 of the device. This will feature the shape of surrounding buildings, distance and
829 positioning, etc. Field tests will also be conducted to evaluate device performance in
830 actual conditions and assess other factors such as noise, visual and related
831 parameters. Economic analysis of the integration of the WIFEH in buildings will be
832 carried out and compared with more established low-energy generation technologies.
833

834 **NOMENCLATURE**

835 **Symbols**

836	U	Air velocity (m/s)
837	H	Height (m)
838	k_s	sand-grain roughness height (m)
839	c_s	roughness constant
840	z_0	Aerodynamic roughness length (m)
841	F1, F2, F3	Front WIFEHs
842	S1, S2, S3	Side WIFEHs
843	R1, R2, R3	Roof WIFEHs

844

845

846 **Acknowledgement**

847

848 We would like to thank the British Council and Department of Science and Technology
849 for the funding (DOST-Newton Fund no.209559487) of this research.

850

851 **REFERENCES**

852

853 [1] Pérez-Lombard, L., Ortiz, J., and Pout, C., “A review on buildings energy
854 consumption information,” *Energy and Buildings*, vol. 40, no. 3, pp. 394–
855 398, 2008.

856 [2] Hu, Y., Zhang, Y., Xu, C., Lin, L., Snyder, R. L., and Wang, Z. L., “Self-
857 powered system with wireless data transmission,” *Nano Letters*, vol. 11, no.
858 6, pp. 2572–2577, Jun. 2011.

859 [3] Zhu, G., Yang, R., Wang, S., and Wang, Z., “Flexible high-output
860 nanogenerator based on lateral ZnO nanowire array,” *Nano Letters*, vol. 10,
861 no. 8, pp. 3151–3155, 2010.

862 [4] Hu, Y., Zhang, Y., Xu, C., Zhu, G., and Wang, Z., “High-output
863 nanogenerator by rational unipolar assembly of conical nanowires and its
864 application for driving a small liquid crystal display,” *Nano Letters*, vol. 10,
865 no. 12, pp. 5025–5031, 2010.

866 [5] Arioli, G. and Gazzola, F., “A new mathematical explanation of what
867 triggered the catastrophic torsional mode of the Tacoma Narrows Bridge,”
868 *Applied Mathematical Modelling*, vol. 39, no. 2, pp. 901–912, 2015.

869 [6] Wang, D., Chiu, C., and Pham, H., “Electromagnetic energy harvesting
870 from vibrations induced by Kármán vortex street,” *Mechatronics*, vol. 22,
871 no. 6, pp. 746–756, 2012.

872 [7] Nguyen, H., Pham, H., and Wang, D., “A miniature pneumatic energy
873 generator using Kármán vortex street,” *Journal of Wind Engineering and
874 Industrial Aerodynamics*, vol. 116, pp. 40–48, 2013.

875 [8] McCarthy, J., Watkins, S., and Deivasigamani, A., “An investigation of
876 fluttering piezoelectric energy harvesters in off-axis and turbulent flows,”
877 *Journal of Wind Engineering and Industrial Aerodynamics*, vol. 136, pp.
878 101–113, 2015.

879 [9] Raghavan, K. and Bernitsas, M., “Experimental investigation of Reynolds
880 number effect on vortex induced vibration of rigid circular cylinder on
881 elastic supports,” *Ocean Engineering*, vol. 38, no. 5, pp. 719–731, 2011.

882 [10] Norberg, C., “Fluctuating lift on a circular cylinder: review and new
883 measurements,” *Journal of Fluids and Structures*, vol. 17, no. 1, pp. 57–96,
884 2003.

885 [11] Sarpkaya, T., “A critical review of the intrinsic nature of vortex-induced
886 vibrations,” *Journal of Fluids and Structures*, vol. 19, no. 4, pp. 389–447,

- 887 2004.
- 888 [12] Tan, Y., Zhu, D., and Beeby, S., “Wind energy harvesting for recharging
889 wireless sensor nodes: brief review and a case study,” in *Rechargeable
890 Sensor Networks: Technology, Theory, and Application*, 2014, pp. 1–30.
- 891 [13] Orrego, S., Shoele, K., Ruas, A., Doran, K., Caggiano, B., Mittal, R., and
892 Kang, S. H., “Harvesting ambient wind energy with an inverted
893 piezoelectric flag,” *Applied Energy*, vol. 194, pp. 212–222, 2017.
- 894 [14] Xiong, H. and Wang, L., “Piezoelectric energy harvester for public
895 roadway: On-site installation and evaluation,” *Applied Energy*, vol. 174, pp.
896 101–107, 2016.
- 897 [15] Sue, C. Y. and Tsai, N. C., “Human powered MEMS-based energy harvest
898 devices,” *Applied Energy*, vol. 93, pp. 390–403, 2012.
- 899 [16] Yole Développement, “Emerging Energy Harvesting Devices,” 2012.
- 900 [17] Han, N., Zhao, D., Schluter, J. U., Goh, E. S., Zhao, H., and Jin, X.,
901 “Performance evaluation of 3D printed miniature electromagnetic energy
902 harvesters driven by air flow,” *Applied Energy*, vol. 178, pp. 672–680, 2016.
- 903 [18] Pimentel, D., Musilek, P., Knight, A., and Heckenbergerova, J.,
904 “Characterization of a wind flutter generator,” in *2010 9th Conference on
905 Environment and Electrical Engineering, EEEIC 2010*, 2010, pp. 81–84.
- 906 [19] Arroyo, E., Foong, S., and Maréchal, L., “Experimental study of an omni-
907 directional wind fluttering energy harvester,” in *ASME 2014 Dynamic
908 Systems and Control Conference*, 2014, p. V003T53A002-V003T53A002.
- 909 [20] Dinh Quy, V., Van Sy, N., Tan Hung, D., and Quoc Huy, V., “Wind tunnel
910 and initial field tests of a micro generator powered by fluid-induced flutter,”
911 *Energy for Sustainable Development*, vol. 33, pp. 75–83, 2016.
- 912 [21] Fei, F., Mai, J., and Li, W., “A wind-flutter energy converter for powering
913 wireless sensors,” *Sensors and Actuators A: Physical*, vol. 173, no. 1, pp.
914 163–171, 2012.
- 915 [22] Zhu, D., Beeby, S., Tudor, J., White, N., and Harris, N., “A novel miniature
916 wind generator for wireless sensing applications,” in *Sensors*, 2010 IEEE,
917 2010, pp. 1415–1418.
- 918 [23] Wang, X., Pan, C. C. L., Liu, Y. Y. Bin, and Feng, Z. H., “Electromagnetic
919 resonant cavity wind energy harvester with optimized reed design and
920 effective magnetic loop,” *Sensors and Actuators, A: Physical*, vol. 205, pp.

- 921 63–71, 2014.
- 922 [24] Kim, S. S., Ji, C., Galle, P., Herrault, F., Wu, X., Lee, J., Choi, C., and Allen,
923 M. G., “An electromagnetic energy scavenger from direct airflow,” *Journal*
924 *of Micromechanics and Microengineering*, vol. 19, no. 9, p. 94010, 2009.
- 925 [25] Munaz, A. and Chung, G.-S., “An electromagnetic energy harvester based
926 on multiple magnet scavenging power from low frequency vibration,”
927 *Microsystem Technologies*, pp. 1–9, 2015.
- 928 [26] Kwon, S., Kim, K., and Lee, S., “Energy Harvesting from Aeroelastic
929 Flutter,” in *The 2012 World Congress on Advances in Civil, Environmental,*
930 *and Materials Research (ACEM’ 12)*, 2012.
- 931 [27] Park, J., Kim, K., Kwon, S., Law, K. H., and Engineering, C., “An aero-
932 elastic flutter based electromagnetic energy harvester with wind speed
933 augmenting funnel,” in *Proceedings of the International Conference on*
934 *Advances in Wind and Structures*, 2012, pp. 26–29.
- 935 [28] Arroyo, E., Foong, S., and Wood, K. L., “Modeling and experimental
936 characterization of a fluttering windbelt for energy harvesting,” *Journal of*
937 *Physics: Conference Series*, vol. 557, no. 1, p. 12089, 2014.
- 938 [29] Toja-Silva, F., Peralta, C., Lopez-Garcia, O., Navarro, J., and Cruz, I., “On
939 Roof Geometry for Urban Wind Energy Exploitation in High-Rise
940 Buildings,” *Computation*, vol. 3, no. 2, pp. 299–325, 2015.
- 941 [30] Calautit, J. K., Chaudhry, H. N., Hughes, B. R., and Sim, L. F., “A validated
942 design methodology for a closed-loop subsonic wind tunnel,” *Journal of*
943 *Wind Engineering and Industrial Aerodynamics*, vol. 125, pp. 180–194,
944 2014.
- 945 [31] Sofotasiou, P., Calautit, J. K., Hughes, B. R., and O’Connor, D., “Towards
946 an integrated computational method to determine internal spaces for
947 optimum environmental conditions,” *Computers & Fluids*, vol. 127, pp.
948 146–160, 2016.
- 949 [32] Tominaga, Y., Akabayashi, S., Kitahara, T., and Arinami, Y., “Air flow
950 around isolated gable-roof buildings with different roof pitches: Wind
951 tunnel experiments and CFD simulations,” *Building and Environment*, vol.
952 84, pp. 204–213, 2015.
- 953 [33] Franke, J., Hellsten, A., Schlünzen, H., Carissimo, B., Baklanov, A.,
954 Barmpas, P., Bartzis, J., Batchvarova, E., Baumann-Stanzer, K., Berkowicz,
955 R., Borrego, C., Britter, R., Brzozowski, K., Burzynski, J., Margarida Costa,
956 A., Dimitrova, R., Grawe, D., Goricsan, I., Janour, Z., Karppinen, A.,

- 957 Ketzel, M., Krajcovicova, J., Leidl, B., Martilli, A., Moussiopoulos, N.,
958 Neophytou, M., Olesen, H., Papachristodoulou, C., Papadakis, M., Piringer,
959 M., Di Sabatino, S., Sandberg, M., Schatzmann, M., and Trini-Castelli, S.,
960 “Best practice guideline for the CFD simulation of flows in the urban
961 environment,” 2007.
- 962 [34] Chaudhry, H., Calautit, J., and Hughes, B., “Computational analysis of a
963 wind tower assisted passive cooling technology for the built environment,”
964 *Journal of Building Engineering*, vol. 1, pp. 63–71, 2015.
- 965 [35] Calautit, J. and Hughes, B., “Wind tunnel and CFD study of the natural
966 ventilation performance of a commercial multi-directional wind tower,”
967 *Building and Environment*, vol. 80, pp. 71–83, 2014.
- 968 [36] Calautit, J., O’Connor, D., and Hughes, B., “Determining the optimum
969 spacing and arrangement for commercial wind towers for ventilation
970 performance,” *Building and Environment*, vol. 82, pp. 274–287, 2014.
- 971 [37] Roache, P., “Conservatism of the GCI in Finite Volume Computations on
972 Steady State Fluid Flow and Heat Transfer,” *ASME J. Fluids Eng.*, vol. 125,
973 pp. 731–732, 2003.
- 974 [38] Celik, I., Ghia, U., and Roache, P., “Procedure for estimation and reporting
975 of uncertainty due to discretization in {CFD} applications,” *Journal of*
976 *fluids {Engineering-*, 2008.
- 977 [39] Roache, P., “A method for uniform reporting of grid refinement studies,”
978 *ASME-PUBLICATIONS-FED*, 1993.
- 979 [40] Tominaga, Y., Mochida, A., Yoshie, R., Kataoka, H., Nozu, T., Yoshikawa,
980 M., and Shirasawa, T., “AIJ guidelines for practical applications of CFD to
981 pedestrian wind environment around buildings,” *Journal of Wind*
982 *Engineering and Industrial Aerodynamics*, vol. 96, no. 10–11, pp. 1749–
983 1761, 2008.
- 984 [41] Launder, B. and Spalding, D., “The numerical computation of turbulent
985 flows,” *Computer methods in applied mechanics and engineering*, vol. 3,
986 no. 2, pp. 269–289, 1974.
- 987 [42] Cebeci, T. and Bradshaw, P., *Momentum transfer in boundary layers*.
988 Washington, DC, Hemisphere Publishing Corp.; New York, McGraw-Hill
989 Book Co, 1977.
- 990 [43] Blocken, B., Stathopoulos, T., and Carmeliet, J., “CFD simulation of the
991 atmospheric boundary layer: wall function problems,” *Atmospheric*
992 *environment*, vol. 41, no. 2, pp. 238–252, 2007.

993
994

Table 1. Sample calculations of discretisation error using the GCI method

	Velocity at height = 3.024m	Velocity at height = 3.021m	Velocity at height = 3.012m
C₁, C₂, C₃	5.9 million, 3.5 million, 2million elements	5.9 million, 3.5 million, 2million elements	5.9 million, 3.5 million, 2million elements
r₂₁	1.29835	1.29835	1.29835
r₃₂	1.3228	1.3228	1.3228
∅₁	2.7134	4.44694	3.73981
∅₂	2.80474	4.44386	3.7654
∅₃	2.9764	4.39079	3.74622
p	2.0689	10.1268	1.0609
∅_{ext}²¹	2.5859	4.4472	3.6596
e_a²¹	3.36%	0.070%	0.68%
e_{ext}²¹	2.58%	0.005%	2.19%
GCI_{fine}²¹	5.87%	0.007%	2.68%

995
996
997
998

Table 2. Summary of the CFD model boundary conditions

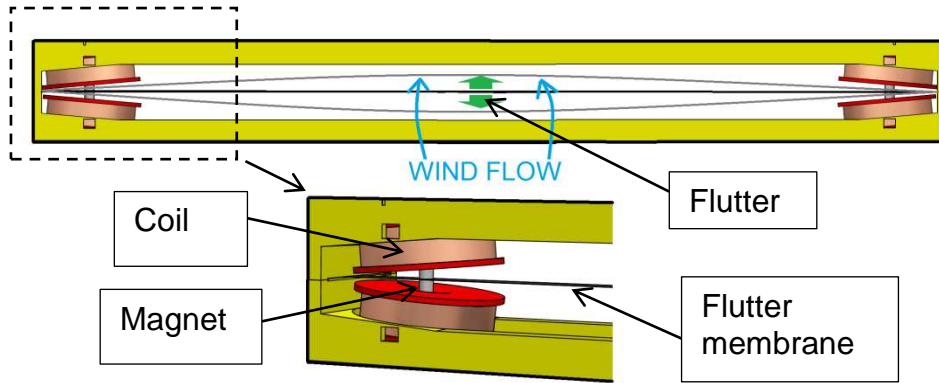
Boundary condition	Set value
Algorithm	SIMPLE
Time	Steady state
Solver type	Pressure based
Discretisation Scheme	Second order upwind
Turbulence model	Standard k-epsilon
Wall boundaries	Standard wall functions
Wall boundaries (Ground)	Modified for roughness Roughness height K _s (m): 0.001 Roughness constant C _{Ks} : 0.5
	Macro-micro climate walls: 0.001
Wall (Sides)	Symmetry (zero normal velocity and zero gradients)
Wall (Top)	Symmetry (zero normal velocity and zero gradients)
Velocity inlet (m/s) at UH	2-10
Wind angle (°)	0-90
Pressure outlet (Pa)	0 (atmospheric)

Gravity (m/s²)

-9.81

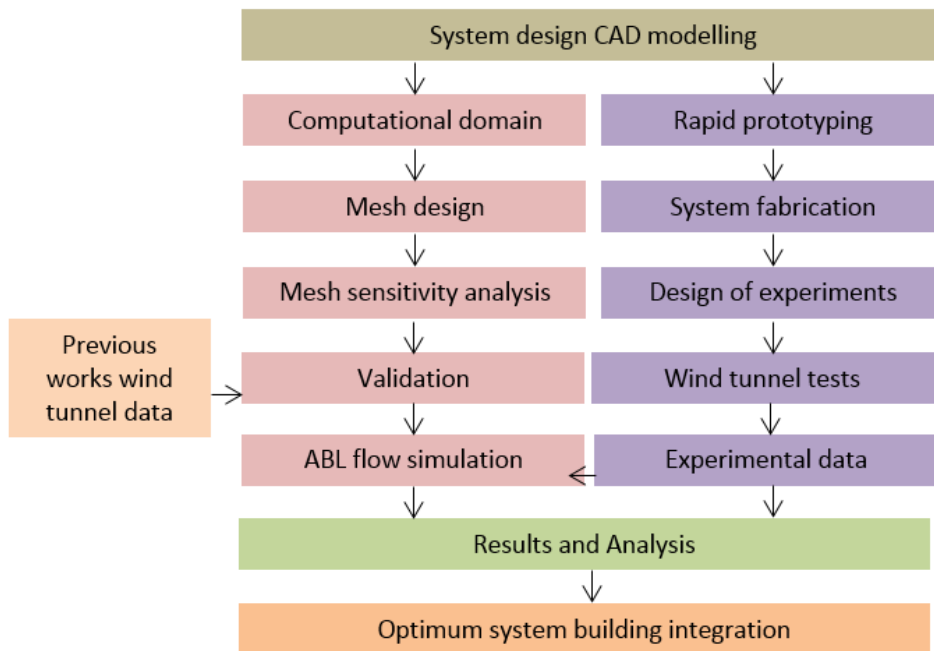
- 999
- 1000
- 1001
- 1002
- 1003
- 1004
- 1005
- 1006
- 1007
- 1008
- 1009
- 1010
- 1011
- 1012
- 1013
- 1014
- 1015
- 1016
- 1017
- 1018
- 1019
- 1020
- 1021
- 1022
- 1023
- 1024
- 1025
- 1026
- 1027
- 1028
- 1029
- 1030
- 1031
- 1032
- 1033
- 1034
- 1035
- 1036
- 1037
- 1038
- 1039
- 1040
- 1041
- 1042
- 1043
- 1044
- 1045

1046



1047
1048
1049
1050
1051
1052

Fig. 1. Schematic diagram of a quad (4-coil arrangement) Wind-Induced Flutter Energy Harvester (WIFEH)



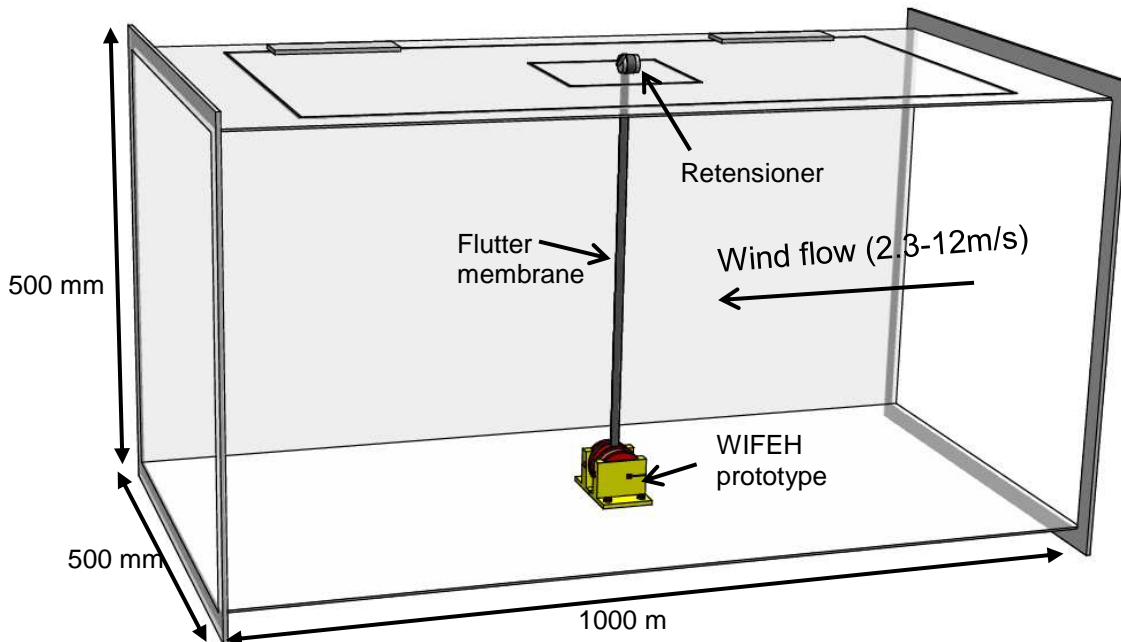
1053
1054
1055
1056
1057
1058
1059
1060
1061
1062
1063
1064

Fig. 2. General organisation of the study



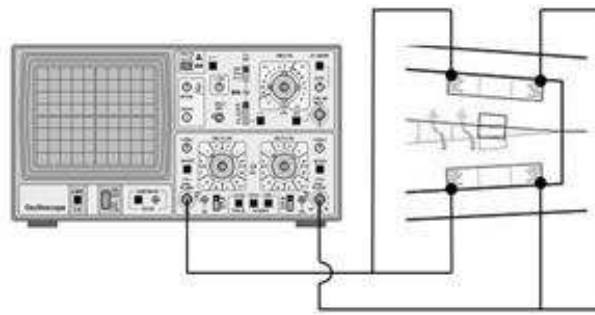
1065
1066
1067
1068
1069
1070

Fig. 3. (a) Side view of the closed-loop wind tunnel (b) WIFEH prototype with one coil configuration showing flutter motion at 2.3 m/s



1071
1072
1073
1074
1075

Fig. 4. Schematic of WIFEH prototype in the wind tunnel test section



1076
1077

Fig. 5. Schematic of the coil connections to the oscilloscope

1078
1079
1080
1081

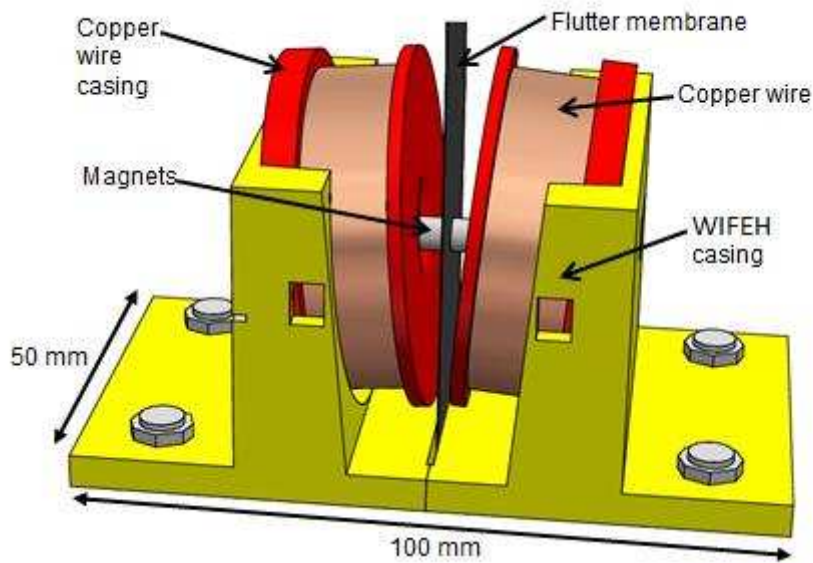


Fig. 6. Schematic and dimensions of 3D-printed WIFEH prototype

1082
1083
1084
1085
1086

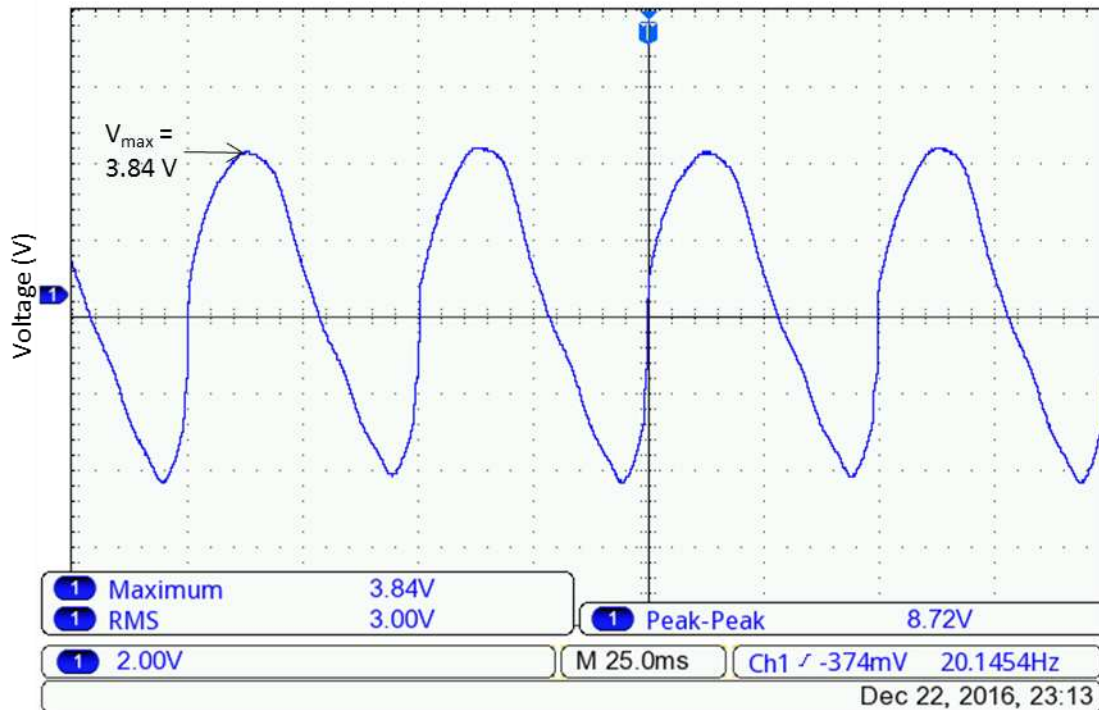
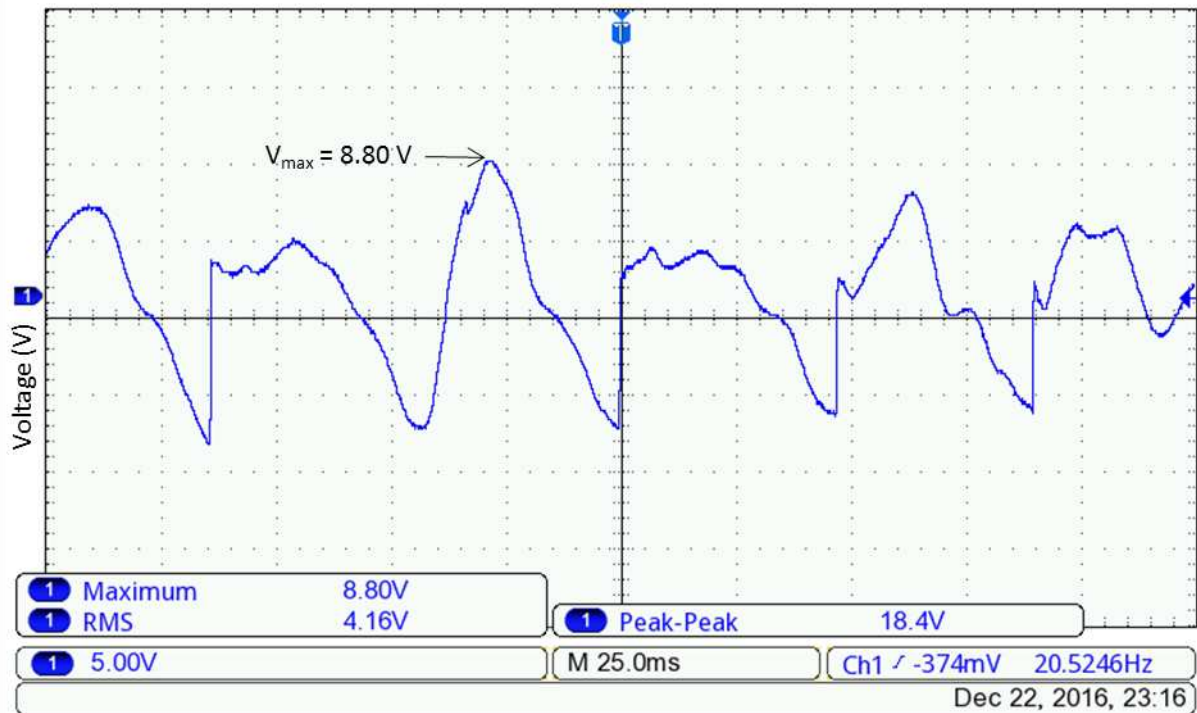


Fig. 7. Open-circuit voltage of the Wind-Induced Flutter Energy Harvester (WIFEH) without membrane retensioning under 2.3 m/s flow velocity

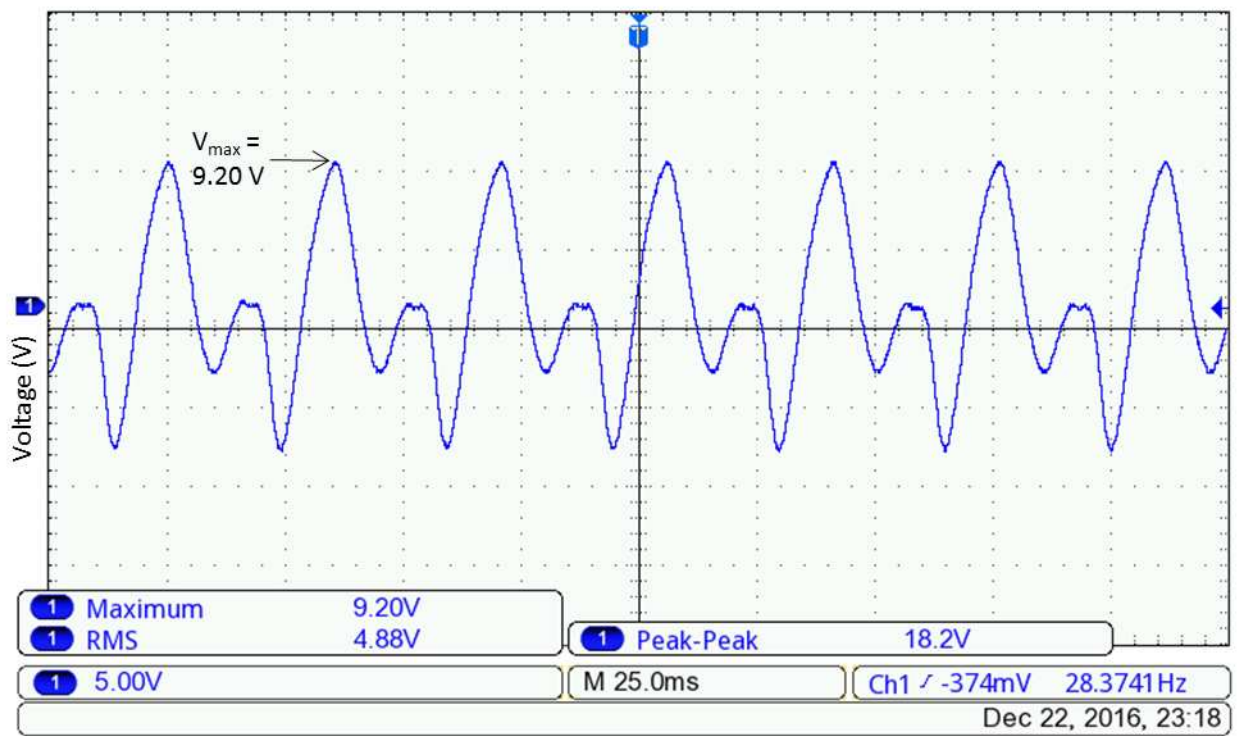
1087
1088
1089
1090
1091
1092

1093
1094
1095
1096



1097
1098
1099
1100
1101

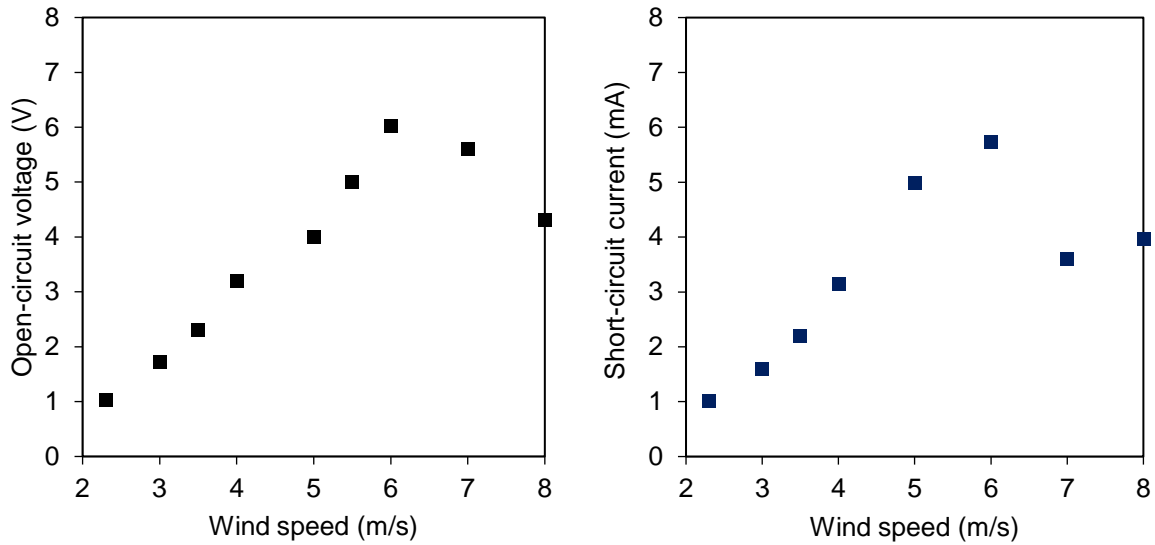
Fig. 8. Electrical signal open-circuit voltage of the Wind-Induced Flutter Energy harvester (WIFEH) without membrane retensioning under 5m/s flow velocity



1102
1103

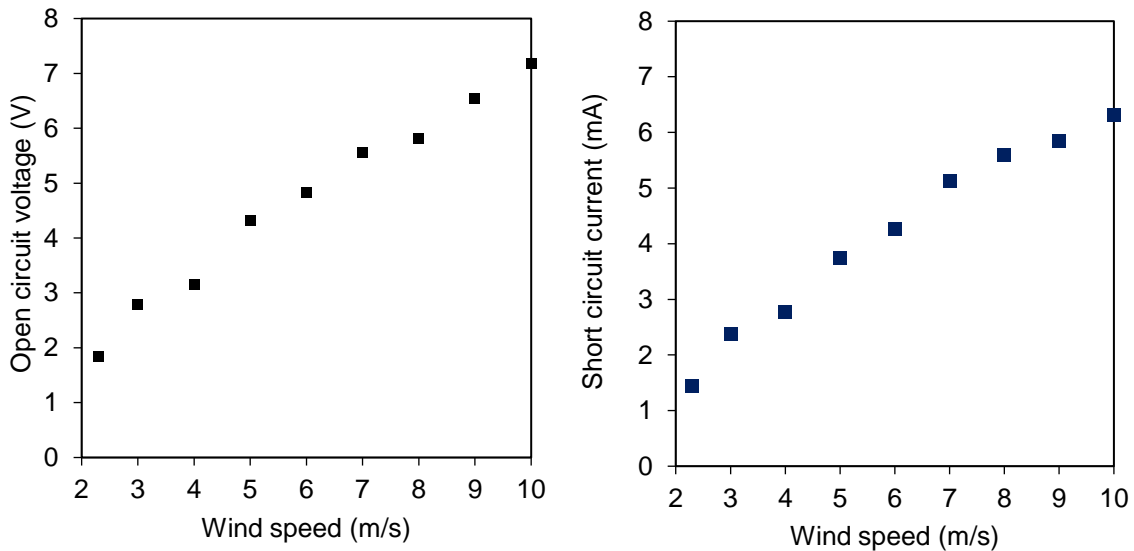
1104
1105
1106

Fig. 9. Electrical signal open-circuit voltage of the Wind-Induced Flutter Energy Harvester (WIFEH) with membrane retensioning under 5 m/s flow velocity



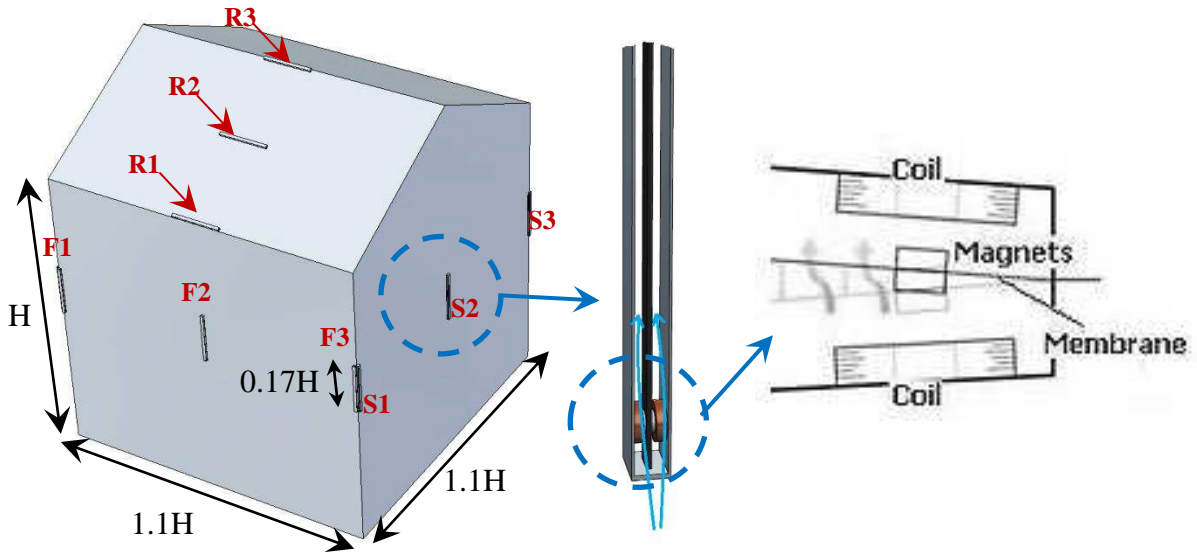
1107
1108
1109
1110
1111
1112
1113

Fig. 10. Electrical output performance of the WIFEH without retensioning under various flow velocities: (a) Open-circuit voltage (b) Short-circuit current



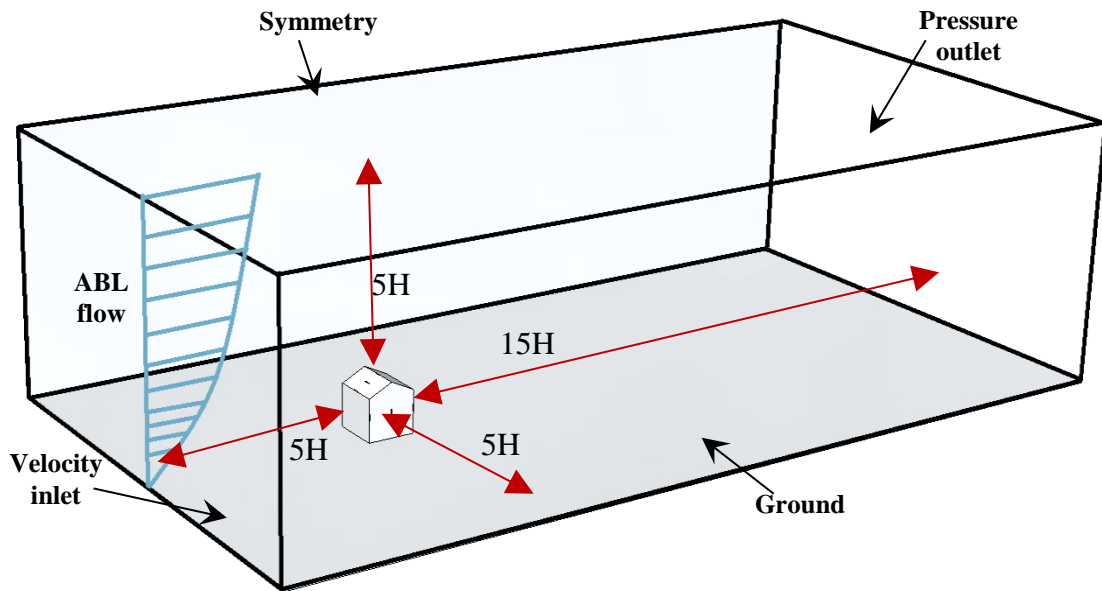
1114
1115
1116
1117
1118
1119

Fig. 11. Electrical output performance of the WIFEH with retensioning under various flow velocities: (a) Open-circuit voltage (b) Short-circuit current



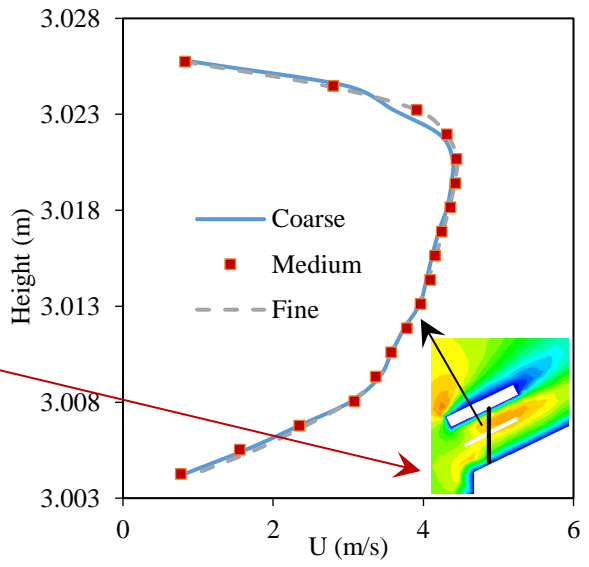
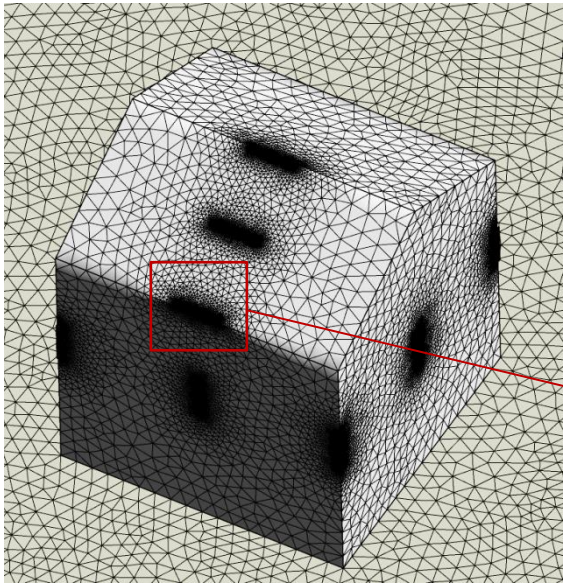
1120
1121
1122

Fig. 12. CAD geometry of building with WIFEH devices



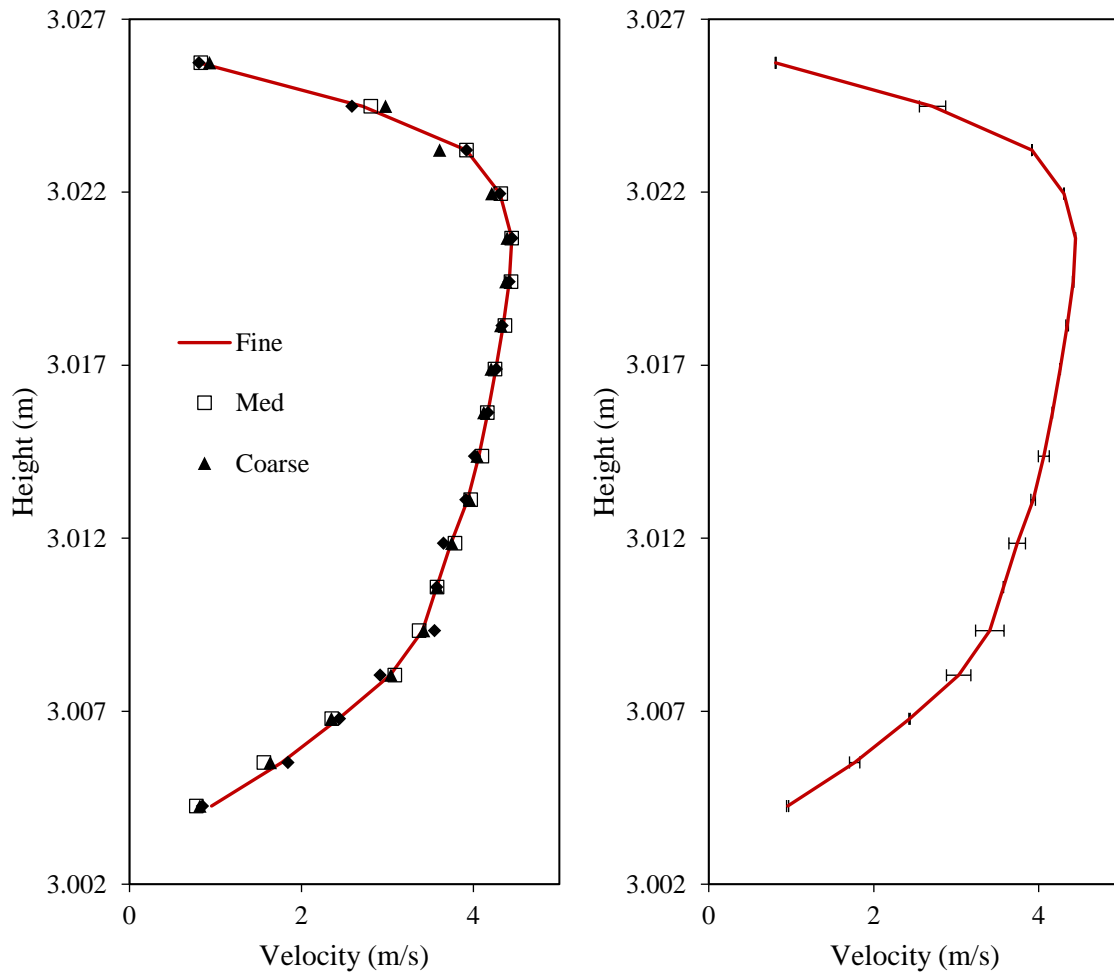
1123
1124
1125
1126

Fig. 13. Computational domain of building with WIFEH devices



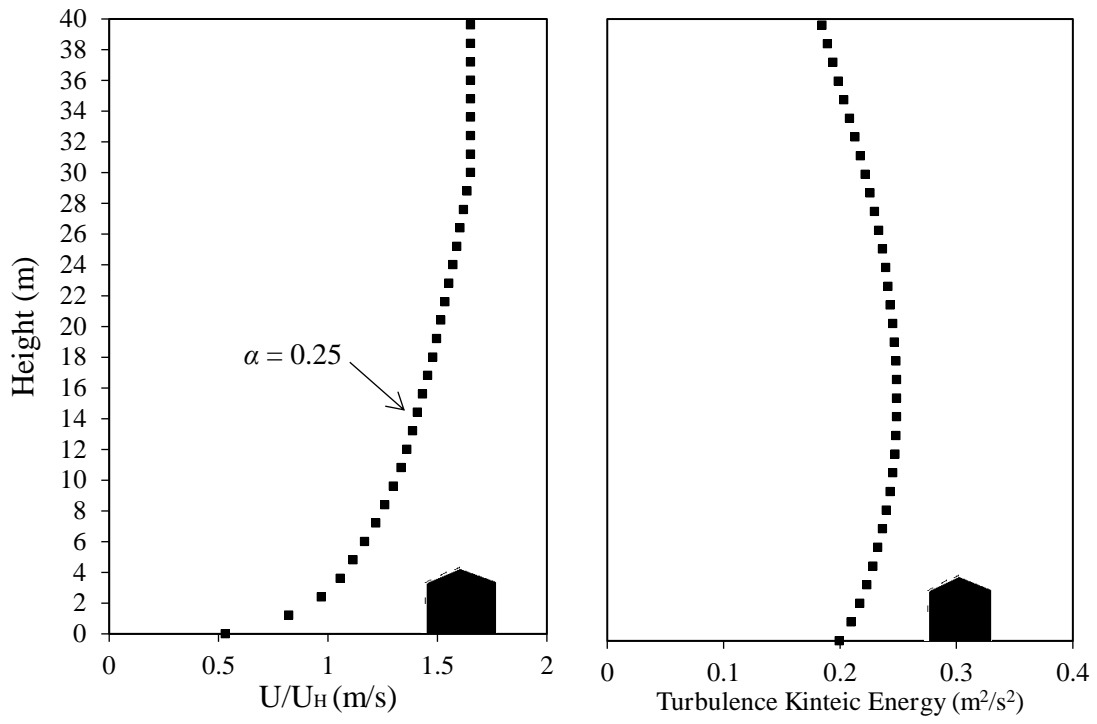
1127
1128
1129
1130

Fig. 14. (a) Computational grid (b) Sensitivity analysis



1132
 1133
 1134
 1135
 1136
 1137

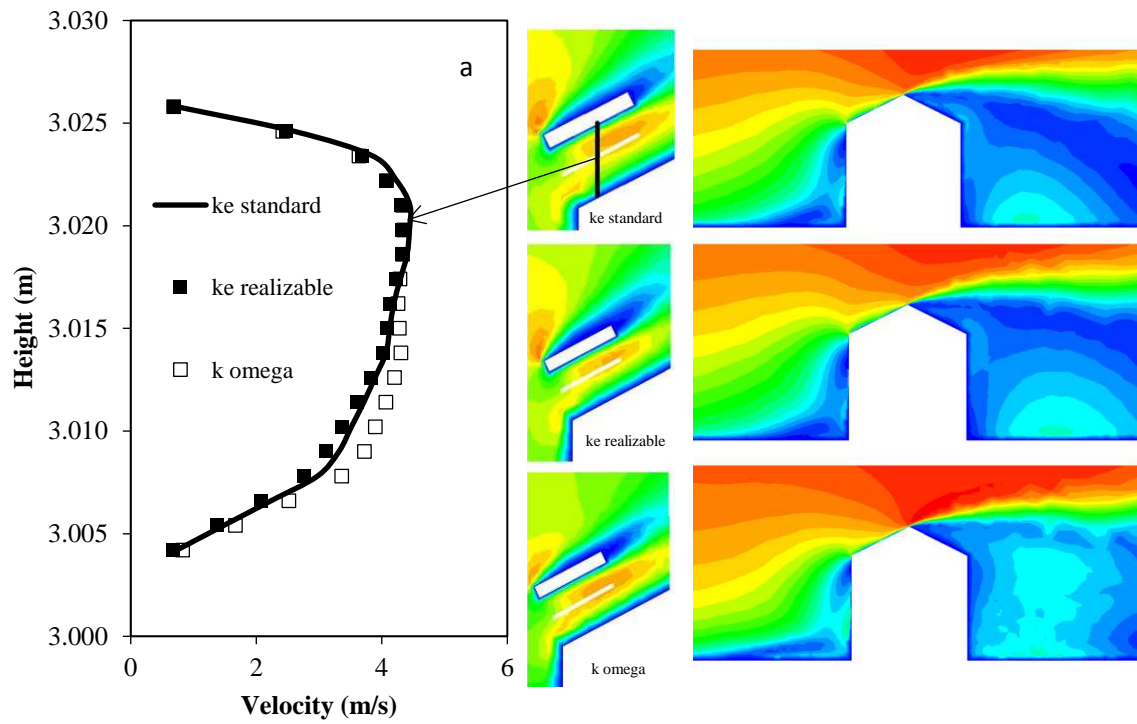
Fig. 15. Grid verification using the Grid Convergence (GCI) method. (a) plot of the velocity profiles drawn from a line in the R1 device; (b) fine grid solution, with discretisation error bars computed using the GCI index.



1138
 1139
 1140
 1141
 1142

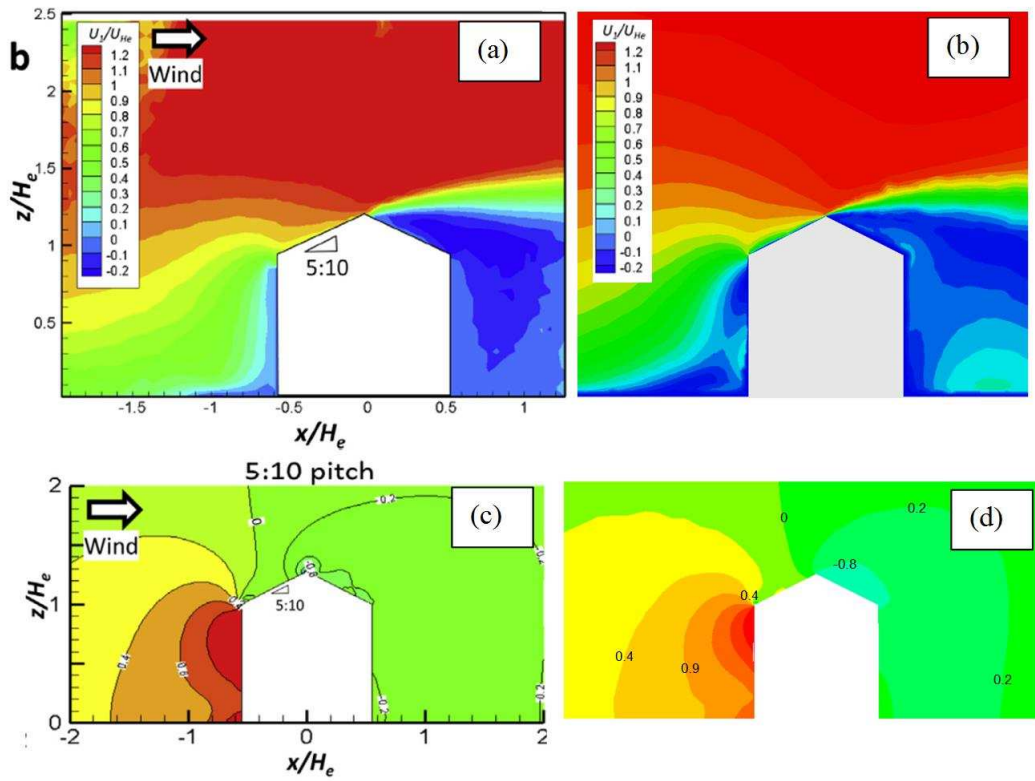
Fig. 16. (a) Velocity profile (b) TKE profile of approach wind flow [29]

1143
1144
1145



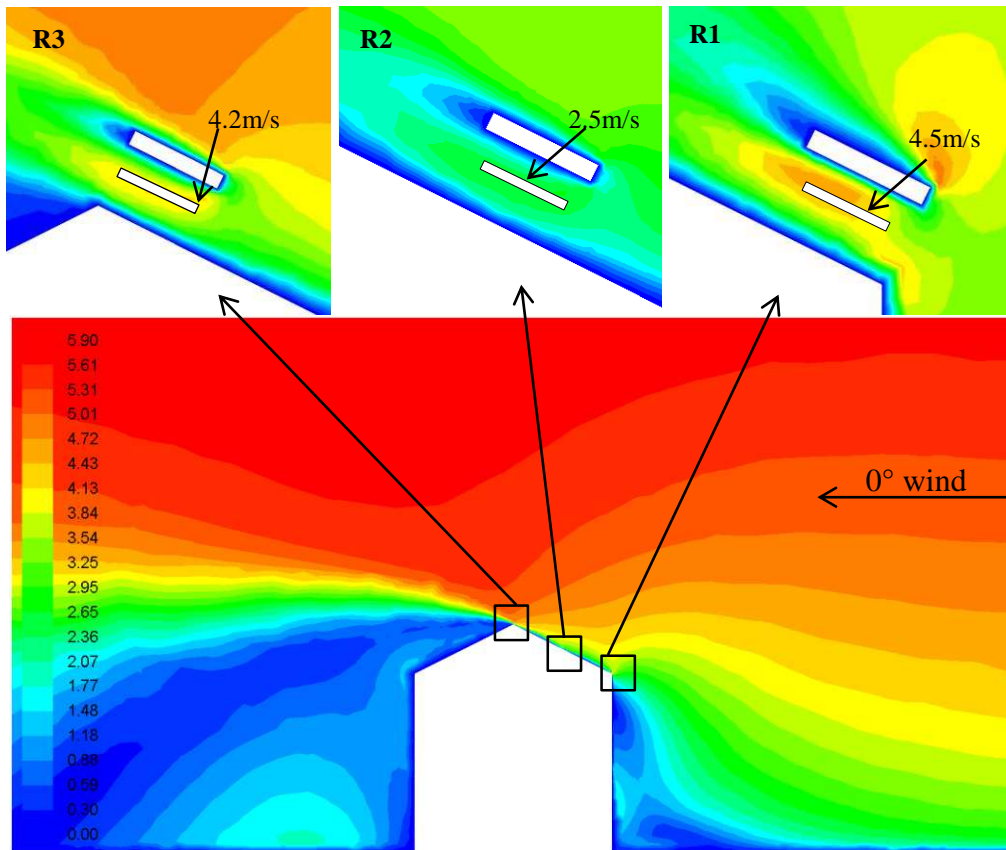
1146
1147
1148
1149
1150
1151
1152

Fig. 17. Sensitivity analysis of turbulence model (a) velocity profile in R1 (b) velocity contours



1153
 1154
 1155
 1156
 1157

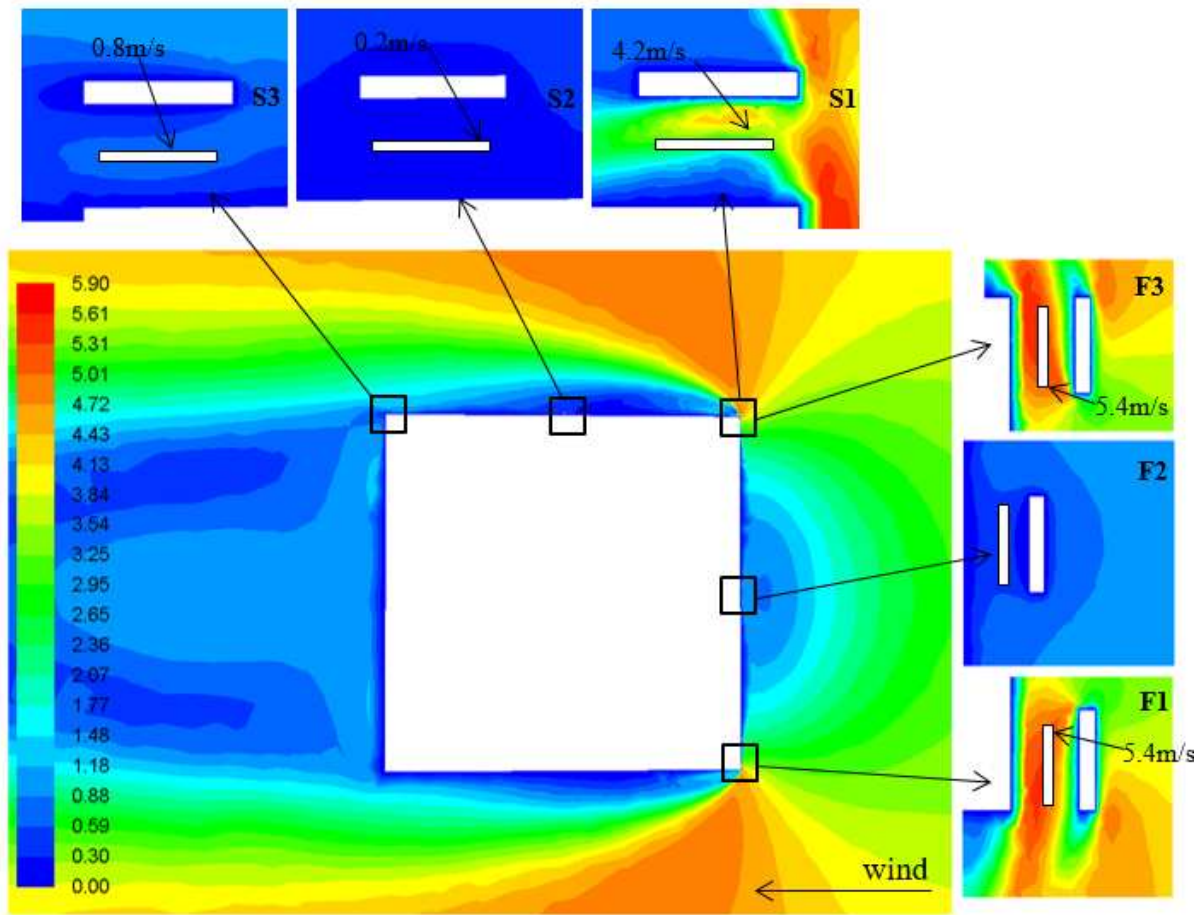
Fig. 18. (a) PIV measurements of velocity [29] (b) velocity distribution in the current model (c) pressure coefficient result [29] (d) pressure coefficient distribution in the current model



1158
 1159

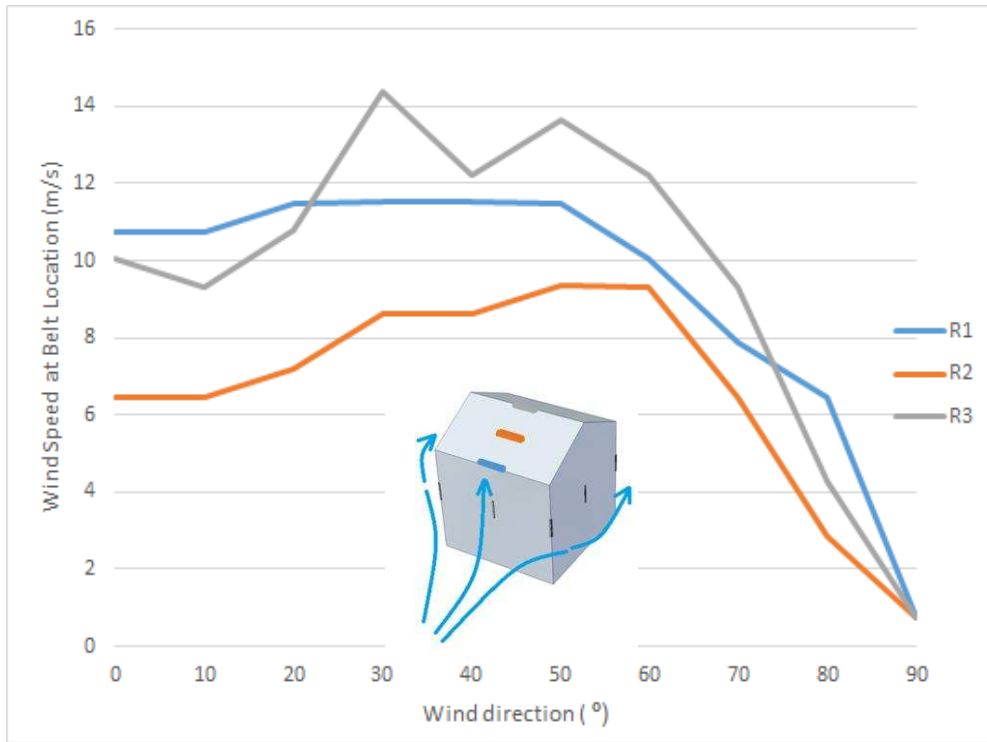
1160
1161
1162

Fig. 19. Contours of velocity magnitude showing a cross-sectional side view of the building



1163
1164
1165
1166

Fig. 20. Contours of velocity magnitude showing a cross-sectional top view of the building



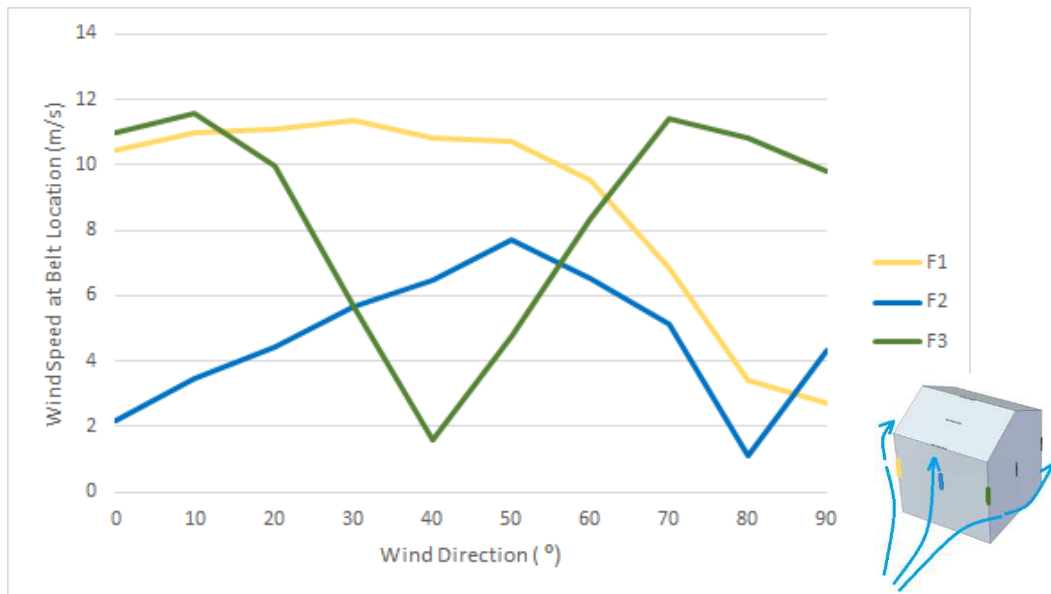
1167

1168 Fig. 21. Effect of wind direction on the wind speed at WIFEH located on the roof for
 1169 various wind angle of approach with outdoor wind $U_H = 10$ m/s

1170

1171

1172

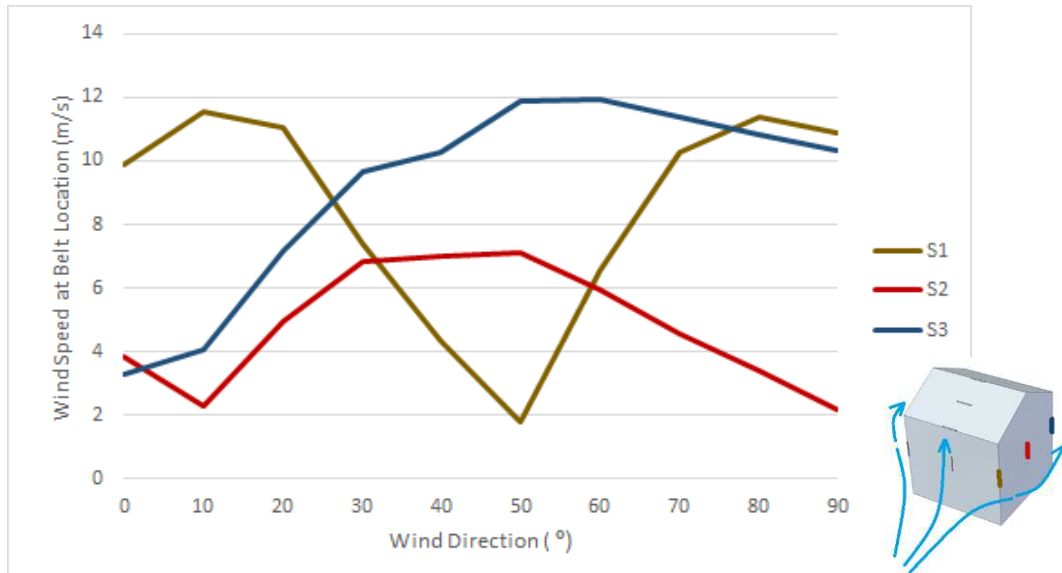


1173

1174 Fig. 22. Effect of wind direction on the wind speed at WIFEH located on the windward
 1175 side of building with outdoor wind at $U_H = 10$ m/s

1176

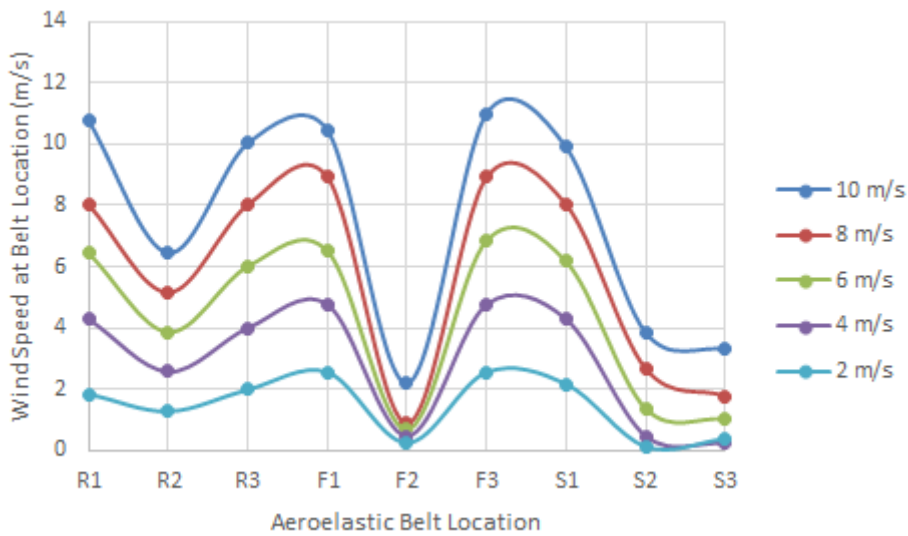
1177



1178
1179

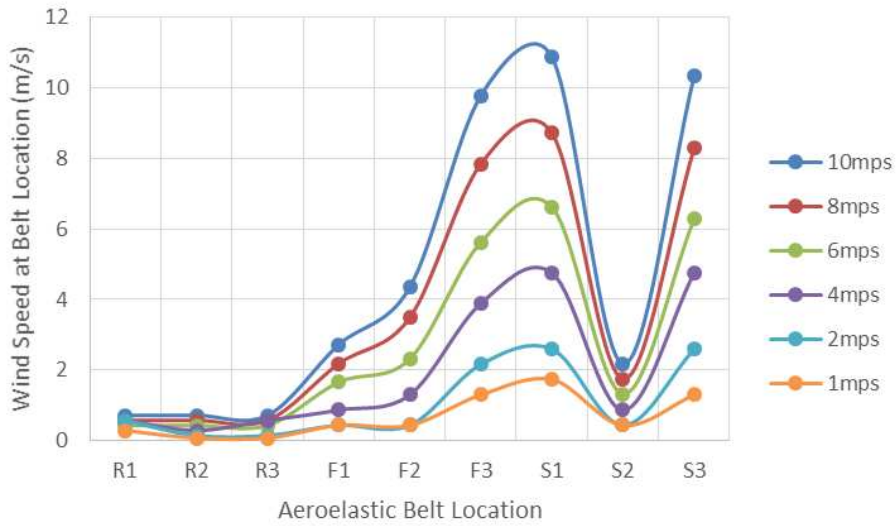
1180 Fig. 23. Effect of wind direction on the wind speed at WIFEH located on the side of
1181 building with outdoor wind at $U_H = 10$ m/s

1182
1183
1184
1185
1186

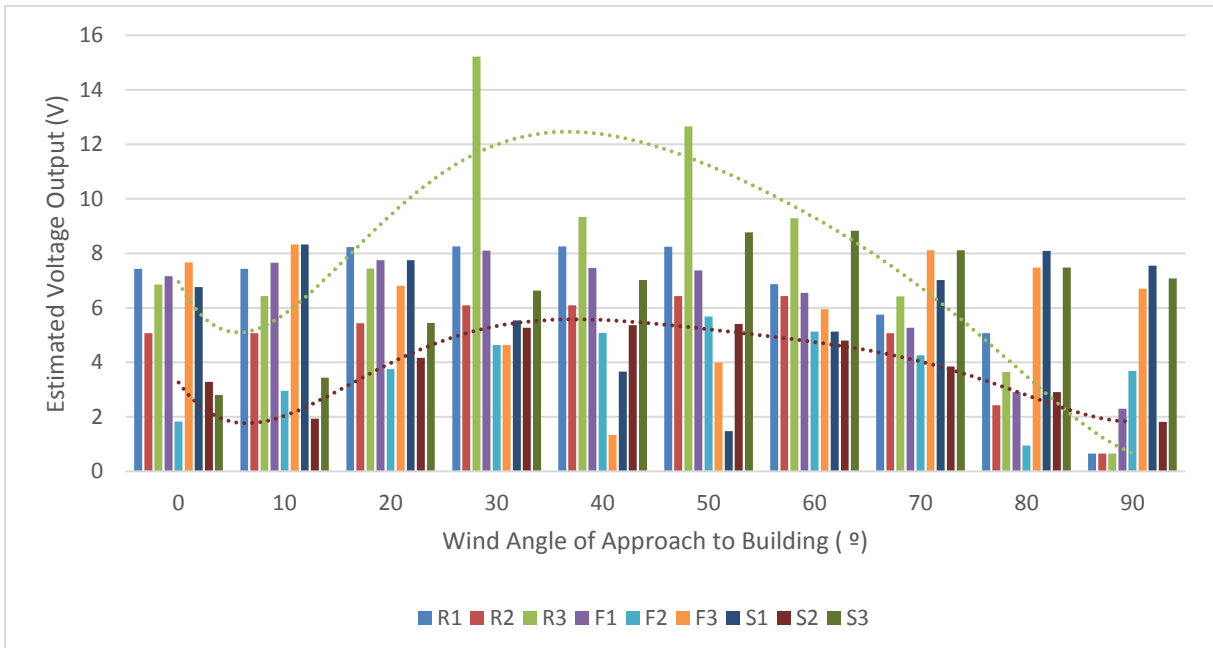


1187
1188
1189
1190

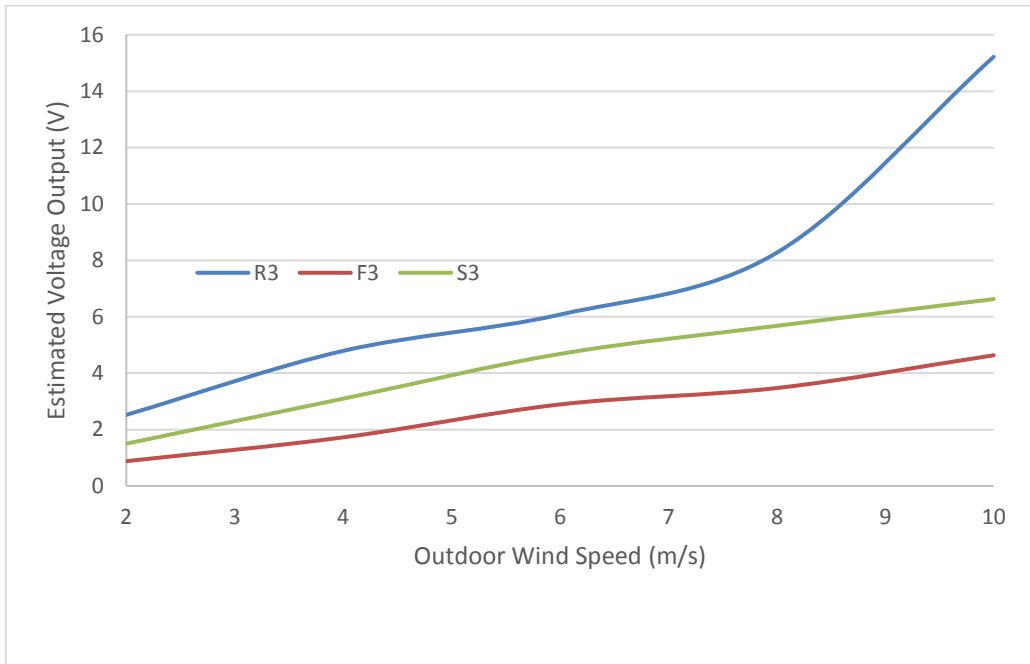
1187 Fig. 24. Wind speeds gathered at WIFEH position for various mounting locations for
1188 0° wind angle of approach
1189
1190



1191 Fig. 25. Wind speeds gathered at WIFEH position for various mounting locations for
 1192 90°wind angle of approach
 1193
 1194
 1195



1196
 1197 Fig. 26. Sample calculation of estimated voltage output based on WIFEH
 1198 (2-magnet-coil system)
 1199



1200

1201

Fig. 27. Impact of various outdoor wind speeds (U_H) on the estimated output of the WIFEH for locations F3, S3 and R3

1202

1203

1204

1205

1206

1207